U. S. DEPARTMENT OF THE INTERIOR
U. S. GEOLOGICAL SURVEY

HIGH RESOLUTION MAPPING OF STRATIGRAPHY USING SEISMIC TOMOGRAPHY: A FEASIBILITY TEST AT THE M-AREA BASIN, SAVANNAH RIVER SITE, SOUTH CAROLINA

by

Karl J. Ellefsen[1]

Open File Report 95-518

---

[1] U. S. Geological Survey, MS 964, Box 25046, Denver, CO 80225

1995

ABSTRACT

At the M-Area basin, Savannah River Site, the saturated and unsaturated zones have been contaminated with dense non-aqueous phase liquids (DNAPLs). The remediation will cost less and require less time if the stratigraphy is known in detail because it strongly affects the migration and emplacement of the contaminants. For this reason, seismic tomography was tested to determine if it could be used to map the stratigraphy near monitoring wells.

The test involved three experiments. For the first, the unsaturated zone was probed using sources on the surface and receivers in a fluid-filled monitoring well. The size of the smallest heterogeneity that could be resolved was approximately 10 ft, which is much greater than the thickness of the major sedimentary layers, and hence seismic tomography with this configuration will not be a useful tool for mapping the sediments. For the second experiment, the unsaturated zone was again probed but using sources and receivers in two fluid-filled monitoring wells. The resolution was approximately 3 ft, and changes in the velocities were well correlated with the fine-scale stratigraphy. For this configuration, seismic tomography can be used for detailed mapping if the wells are close together (i.e., within approximately 20 ft). For the third experiment, the saturated zone was probed using sources and receivers in two fluid-filled monitoring wells. The resolution was about 3 ft, and velocities were also well correlated with the stratigraphy. In the saturated zone, seismic tomography can be a valuable tool for high resolution mapping of stratigraphy even between widely spaced wells (i.e., up to 50 ft apart).

Of the three experiments, the well-to-well tomography in the saturated zone is the best suited to high resolution mapping of stratigraphy. For DNAPL remediation, these maps will be invaluable to hydrologists who are designing alcohol or surfactant injections because the maps show the locations of discontinuous sand and clay layers between wells. These maps will also be needed by geophysicists who are monitoring DNAPL remediation using borehole radar data: once the geophysicists know the geology, they can separate the effects on the waves due to the geology from those due to changes in the pore fluids, and in this way the monitoring should be improved.

CONTENTS

LIST OF FIGURES

LIST OF TABLES

1. INTRODUCTION

At Savannah River Site, which is near Aiken, South Carolina, approximately 2 million pounds of solvents were put into a man-made basin to dispose of them (Westinghouse Savannah River Company, 1992, p. 2). The solvents include trichloroethylene, tetrachloroethylene, and trichloroethane, which are classified as dense non-aqueous phase liquids (DNAPL). From the basin, which is called the "M-Area Settling Basin", the DNAPL migrated into the unsaturated and saturated zones and contaminated the ground water. Since 1987, the contaminated ground water has been monitored and remediated under a Resource Conservation and Recovery Act (RCRA) Part B application. This work was performed as part of a research program for which the purpose was to identify and remediate the separate phase solvent in the ground.

To decrease the cost of removal, methods for characterizing the stratigraphy, which affects the migration of DNAPL, and for monitoring the remediation of DNAPL (Jordan et al., 1993) are needed. To this end, the Branch of Geophysics, U. S. Geological Survey, which is being sponsored by the Department of Energy, is testing different geophysical techniques. Because which techniques would work under the conditions at the Site was not known when the project began, feasibility tests were performed with several that seemed suitable — well-to-well radar, well-to-well and surface-to-well seismic tomography, and complex resistivity. In this report are the results of the seismic tomography.

If the conditions are suitable, seismic tomography can be used to make highly detailed maps of stratigraphy near monitoring wells. These maps should be invaluable during the design of the remediation program because they show the lateral extent of discontinuous sand or clay layers — they show what geologic features might affect the flow of surfactants used for remediation. Furthermore, these maps should help geophysicists interpret radar data, which is important because radar methods have been proposed as a means of monitoring the addition of surfactants or alcohols as part of the remediation process and as a means of monitoring the removal of DNAPL. The problem with using radar methods in this sedimentary environment is that radar waves will be guided by the clay layers (Olhoeft, oral commun., 1994). With seismic tomography, the discontinuities in the clay layers can be located making quantitative interpretation of the radar data feasible.

The purpose of this feasibility test was to delineate the extent to which the site conditions (e.g., attenuation of the waves, mechanical coupling between the well casings and the sediments) affect the tomography. To this end, three objectives were established: (1) Determine whether seismic waves in the unsaturated and saturated zones can be propagated for the distances needed in tomography. If they can, then the second and third objectives would be pursued. (2) Determine the resolution of the tomograms (i.e., the size of the smallest heterogeneity that can be discerned). (3) Determine whether the details in the tomograms correspond to what is known independently about the geology.

This report begins with a discussion of the geology and well construction because this information is needed to understand the wave propagation and to interpret the tomograms. Then the collection and the processing of the data are described. The results from three tomographic experiments — well-to-well acquisition geometry in the saturated zone, well-to-well acquisition geometry in the unsaturated zone, and surface-to-well acquisition geometry in the unsaturated zone — are presented individually. To interpret the tomograms, they are compared to core, geophysical logging, and well-to-well radar data; with this integrated approach a better understanding of the geology is obtained. In the final section are a summary of the results and some recommendations for future investigations.

2. GEOLOGY AND WELL CONSTRUCTION

The feasibility test was performed in unconsolidated sediments consisting of clays, silts, sands, and gravels (Westinghouse Savannah River Company, 1992, p. 18; Eddy-Dilek et al., 1993, p. 11). These sediments were deposited during the Middle to Upper Eocene in shallow marine, lagoonal, fluvial, and flood plain environments, and the strata tend to be discontinuous in the horizontal direction. The entire sedimentary section, which is part of the Atlantic Coast Plain, is approximately 750 ft thick near the M-Area basin. During the feasibility test the elevation of the water table was 232 ft, and so the combined thickness of capillary fringe and unsaturated zones was 126 ft.

To interpret the tomograms, information about the clay mineralogy is needed. Near the M-Area basin, the most abundant clay is kaolinite; illite and smectite are also present but in much smaller quantities (Horton, 1995). Other investigators (DiStefano 1989, Everest Geotech Company, date unknown; Seagull, 1992) who analyzed samples from several parts of the Site found that kaolinite is the most abundant clay and that other clays (i.e., illite, vermiculite, smectite, and halloysite) are present in relatively small quantities.

The feasibility test was performed using the wells on the north side of the M-Area basin (Figure 1a), which extend to different depths in the unsaturated, capillary fringe, and saturated zones (Figure 1b). The locations of the wells are listed in Table 1. The construction of all wells (Figure 2) is similar: The casing is polyvinyl chloride plastic with an inside diameter of 4 in, and the annualar space between the casing and the sediments is filled with grout. The screen is also polyvinyl chloride plastic with an inside diameter of 4 in, and the annualar space between the screen and the sediments is filled with sand. The screen and sandpack are sealed with a 4 ft plug made from coarse sand overlain with bentonite. The borehole diameter, including casing and grout, is approximately 11 in.

3. DATA ACQUISITION

3.1 Seismic Data, Well-to-Well Geometry, Saturated and Unsaturated Zones

For the saturated zone, the seismic source and the hydrophone cable were in wells MSB-3C and MSB-3B, respectively (Figure 1b). For the unsaturated zone, the seismic source and the hydrophone cable were in wells MSB-3A and MSB-3B, respectively (Figure 1b).

For the later experiment, the wells were filled with water after well packers were placed just above the water table.

Seismic waves were generated by the "OWS downhole seismic source" (Oyo Corporation, 1993). The waves were detected with an array consisting of 24 hydrophones, which were spaced 6.56 ft (2.00 m) apart and for which the 3 dB points of the frequency response are 7 Hz and 36 kHz. The data were recorded with the "McSEIS 170f" (Oyo Corporation, 1991), for which the resolution is 12 bits and the gain is set by an internal floating point amplifier. One data channel was reserved for the trigger, a signal from a geophone in the source indicating when the source fired. To combine this channel with the channels from the hydrophone array, a CDP roll-along switch, manufactured by Oyo, was used. The data were stored in a format unique to OYO.

To get the most accurate picks of travel times, the sample rate was set to $25. \times 10^{-6}$ s, the highest rate available with the recording equipment. A total of 12 channels — 11 for the data plus one for the trigger — were recorded because this was the capacity of the recording equipment at this sample rate, and each channel had 2048 samples. With this recording time, the direct wave was in the middle third of each seismogram, making the picking of travel times convenient.

Using test shots collected in the saturated zone, the velocity of *P*-wave propagation was determined to be approximately 5.5×10^3 ft/s (1.7×10^3 m/s), and these data contained frequencies at least as high as 2 kHz. For this situation, the wavelength was approximately 3 ft (1 m), and the size of the Fresnel zone ranged from approximately 1.5 ft (0.5 m) at the wells to 5.0 ft (1.5 m) half way between them. Because the best resolution with transmission tomography is slightly less than the size of the Fresnel zone (Williamson and Worthington, 1993), the spacing between adjacent shots or receivers should be approximately the size of the smallest Fresnel zone. As a reasonable compromise between satisfying this criterion and minimizing the amount of data to be collected, the spacing between successive shots and receivers was chosen to be 1.6 ft (0.50 m). To get this spacing, four shots were recorded at each shot location, and the hydrophone array was moved 1.6 ft (0.50 m) between shots. From test shots in the unsaturated zone, the velocity of *P*-wave propagation was determined to be approximately 2.5×10^3 ft/s (7.6×10^2 m/s), and these data contained frequencies at least as high as 1 kHz. For the shortest wave length, the size of the Fresnel zone ranged from approximately 1.3 ft (0.4 m) at the wells to 3.0 ft (1.0 m) half way between them. As a reasonable compromise, the spacing between successive shots and receivers was chosen to be 1.6 ft (0.50 m).

Typical examples of common shot gathers collected in the saturated and unsaturated zones are shown in Figures 3a and 3b, respectively. The first, large amplitude pulse on each seismogram is the *P*-wave that travels directly from the source to the receiver. The moveout is approximately hyperbolic, which is characteristic of all data collected in the well-to-well geometry. These gathers show two problems with the data that affected the processing. First, receiver number 7 was usually noisy, and this problem might be caused by a poor electrical connection within the cable head (J. Mims, oral commun., 1994).

Second, the CDP roll-along switch sometimes mixed the seismograms from different receivers, as can be seen, for example, in receiver number 12. After the field work was finished, the manufacturer determined that this problem was caused by dirty electrical contacts within the switch. Another problem, which is not evident in the gathers but became apparent after the data were closely scrutized, was that the trigger was irregular: it did not accurately indicate when the source fired. After the field work was finished, the manufacturer determined that this problem was caused by a broken part within the source (T. Kanemori, oral commun., 1994).

3.2 Seismic Data, Surface-to-Well Geometry, Unsaturated Zone

For this experiment, the surface sources were along a line that passed close to well MSB-3B, and their exact locations are listed in Table 2. The waves were generated by a metal plate that was struck with a sledge hammer; a switch attached to the hammer served as the trigger. The hydrophone cable was in well MSB-3B, which was filled with water after a well packer was installed. The same recording equipment that was used for the well-to-well geometry (see Section 3.1) was used for this geometry too.

The sample rate was set to $100. \times 10^{-6}$ s, which was adequate because the highest frequency was approximately 350 Hz. Although all 24 channels were recorded, only 17 had data because only 17 hydrophones could fit in the well. Since each channel had 2048 samples, the total recording time was 0.2047 s, which was long enough to record the direct wave at all offsets. To increase the signal-to-noise ratio, five shots were recorded at each station, and the seismograms were stacked. Using some test shots, the velocity of *P*-wave propagation in the unsaturated zone was determined to be approximately 2.5×10^3 ft/s (7.6×10^2 m/s). If the source and receiver were separated by 69 ft (21 m), which would be a typical distance for this geometry, the size of the Fresnel zone would range from approximately 3.5 ft (1.0 m) at the source or the receiver to 11 ft (3.3 m) half way between them. As a reasonable compromise, the spacing between successive shots and receivers was chosen to be 6.5 ft (2.0 m).

A typical example of a common shot gather is shown in Figure 4. The large amplitude pulse including the smaller precursor is the P-wave that travels directly from the source to the receiver. The moveout is approximately linear, which is typical of seismic data collected in this geometry. With the exception of receiver number 7, the data contain virtually no noise. Again, the cause of the noise on receiver 7 might be a poor electrical connection at the cable head. Unlike the data collected in the well-to-well geometry (see Section 3.1), no mixing of seismograms occurred because the CDP roll-along switch was not used, and no timing problems occurred because the trigger worked well.

3.3 Other Seismic Data

Extra data were collected for the well-to-well geometry (MSB-3B to MSB-58D in the unsaturated zone) and for the surface-to-well geometry (MSB-3B in the saturated zone, MSB-3C in the saturated zone, and MSB-58D in the saturated and unsaturated zones).

When these data were examined, their character was found to be identical to the other data (see Sections 3.1 and 3.2). Since the likelihood of developing new and significant findings from these extra data was low, they were not processed.

3.4 Borehole Deviation Data

Since the locations of the sources and receivers must be accurately known for tomography, the deviations of wells MSB-3A, MSB-3B, MSB-3C, MSB-3D, MSB-22, MSB-58D were measured. (The extra wells, MSB-3D and MSB-22, were measured because well-to-well radar data were collected in these.) The deviations, which were determined with the "Drift Logging System" (Oyo Corporation, 1986), are listed in the Appendix. In all wells used for the tomography, the magnitude of the deviation is almost always less than 0.16 ft (5.0×10^{-2} m); the only significant exception is a 13 ft (4.0 m) interval in well MSB-3B where the magnitude slightly exceeds 0.33 ft (0.10 m). Because these deviations are relatively small compared to the wave lengths, they were ignored during the processing.

4. DATA PROCESSING

4.1 Preparing the Seismograms

The first procedure in the processing, preparing the seismograms, involved four steps. First, each data file was converted from the OYO format to a simple binary file. Second, the seismograms that were contaminated by cross-feed (see Section 3.1) were edited to remove as much of it as possible. To accomplish this, the contaminating seismogram was scaled and then subtracted from the original seismogram; to determine the best scale factor, different values were tried until the amplitude of the cross-feed was minimized. Third, any poor-quality seismograms — usually the seismogram from receiver number 7, which contained too much noise (Figures 3 and 4), and sometimes those seismograms from which the cross-feed could not be removed — were set to zero. Fourth, the data were converted to SEG-Y format (Barry et al., 1980), a standard used throughout the geophysical industry, and the source and receiver coordinates were assigned. Because the boreholes were almost perfectly straight (see Section 3.4), assigning locations was unusually easy: the east and north coordinates for the well were used for the x and y coordinates, respectively; the elevations, which were computed from the elevations in Tables 1 and 2, were used for the z coordinates.

4.2 Determining the Travel Times

Determining the travel times, the second procedure in the processing, involved three steps. First, the travel times were picked for each data file, which was a common shot gather (Yilmaz, 1987, p. 47-48). The advantage of using a gather is that the seismograms can be correlated improving the accuracy of the picks, especially for those seismograms recorded far from the source. The correlations and picks are performed with the human eye; although this approach may seem primitive, the human eye is more accurate than any

machine algorithm is. Also, this approach is a form of quality control: the geophysicist must examine all seismograms and their picks.

Picking the travel times, especially from the seismograms collected in the unsaturated zone, was difficult. The cause was not noise — it was dispersion. This phenomenon is manifested in the seismograms as a change in the shape of the wave with distance and is caused by a monotonic increase in velocity with frequency (Aki and Richards, 1980, p. 167-185). Dispersion can be observed, for example, in a close-up view of some seismograms (Figure 5): Notice that the shapes of the first part of the arriving wave are very similar for receivers 6 and 5. But for receiver 4 and especially for receiver 3, the shape has changed markedly. Because the amount of dispersion increases as the attenuation increases, the dispersion is particularly troublesome in the unsaturated zone where the attenuation is high. Picking the first arrival of the wave was virtually impossible; so the time at the bottom of the first trough in each seismogram was used. Because this time does not correspond to that of first arrival, a time shift, which will be explained next, was used to account for the difference. Whenever the dispersion was too great, the pick was rejected.

Second, a constant time shift or static had to be applied to each shot gather because the time at which the source fired was not known accurately enough and because the picks were on the troughs. To obtain an estimate of this static, an algorithm based on a simple model of the ground was used: the ground between the wells was assumed to be homogeneous. For this model, the rays are straight and may be expressed with this relation: for ray i, the picked time t_i equals the slowness s times the (straight line) distance x_i minus the static t_s. For the entire gather, which has n rays,

$$\begin{pmatrix} t_1 \\ t_2 \\ \vdots \\ t_n \end{pmatrix} = \begin{pmatrix} x_1 & -1 \\ x_2 & -1 \\ \vdots & \vdots \\ x_n & -1 \end{pmatrix} \begin{pmatrix} s \\ t_s \end{pmatrix}.$$

Using the least squares method, this equation was solved for s and t_s, and then t_s was added to the travel times for the gather.

Third, the statics were checked using two criteria: the slowness must change gradually with depth, and at any given depth the slownesses for all four positions of the hydrophone cable (see Section 3.1) must be similar. These conditions were met for all data except for data collected in two positions of the hydrophone cable in the saturated zone. This discrepancy might be caused by an inaccurate recording of the cable's location. The data associated with these two were not used to calculate the tomogram, and the upshot of omitting them is that the resolution of the tomogram near the receiver well is lower than it would be otherwise.

4.3 Estimating the Velocities

Estimating the velocities, the final procedure in the processing, was based on a mathematical model of the ground that was three dimensional, heterogeneous, isotropic, and perfectly elastic. A three dimensional model was needed to process the surface-to-well data because the sources and receivers did not lie in a common plane. For the well-to-well data, a two dimensional model would have been suitable because both wells are practically straight and vertical (see Section 3.4), but the three dimensional model was used anyway. The velocity was allowed to vary in a vertical plane, which in the well-to-well geometry passed through the source and receiver wells and in the surface-to-well geometry passed just through the receiver well, but the velocity was not allowed to vary perpendicular to this plane because such variations cannot be adequately determined given the geometry of the sources and receivers. Isotropy was chosen because it is much simpler than anisotropy and no evidence exists yet that these soils are anisotropic. Perfect elasticity was chosen because no algorithms exist yet to account for anelasticity.

The mathematical model is represented by a grid that covers the sources, the receivers, and the ground between them (Figure 6). At each intersection on the grid, a velocity is assigned, and in between the intersections, the velocity is calculated via interpolation (Block, 1991, p. 21). The spacing of the points is chosen to be approximately equal to the radius of the smallest Fresnel zone (see Section 3.1 and 3.2) because this radius is approximately the size of the smallest heterogeneity that can be resolved (Williamson and Worthington, 1993).

The best velocities for the model are defined to have two characteristics: the travel times predicted with these velocities must be close to the observed travel times, and the velocities may only change smoothly with distance. The second characteristic results from the physics of wave propagation — because the wave tends to average the properties of the sediments over a distance of a wavelength, estimating (with deterministic methods) velocity heterogeneity over shorter distances is very difficult (and has not been done yet). These two characteristics are expressed mathematically using a cost function:

$$c = \left[\mathbf{d} - \mathbf{g}(\mathbf{m})\right]^T \left[\mathbf{d} - \mathbf{g}(\mathbf{m})\right] + \lambda \left[\mathbf{Km}\right]^T \left[\mathbf{Km}\right] .$$

In vector $\mathbf{d}$ are the picked travel times; in vector $\mathbf{g}(\mathbf{m})$ are the predicted travel times, which are calculated with ray tracing (Um and Thurber, 1987) for the current model $\mathbf{m}$. The predicted travel times also include a source static correction (see e. g., Block et al., 1994). Thus the first term is the contribution to the cost due to the mismatch between the observed and predicted travel times. Because matrix $\mathbf{K}$ is a first derivative operator, vector $\mathbf{Km}$ contains the first derivatives of the velocities in the model. Thus, the second term is a measure of the roughness of the model and is needed to constrain the model (Phillips and Fehler, 1991). The contribution of this term to the cost is controlled by λ.

By minimizing c the best velocities are determined. The easiest and most straightforward method of minimization is least squares (see e. g., Lines and Treitel, 1984), and this

method was always used first to obtain an initial estimate of the velocities. However, the solution obtained with the least squares method can be significantly affected by outliers in the data (see e. g., Scales et al., 1988), which in this case are inaccurate travel time picks. To overcome this problem, the minimization was usually repeated using iteratively reweighted least squares (Scales and Gersztenkorn, 1988) for which the starting model was the final solution from the least squares minimization. The norm for this second minimization was chosen to be $l_{1.1}$.

The selection of λ, which controls the contribution of the roughness term to the total cost, is not arbitrary. To determine a suitable value, the minimization is performed with many different values, and the pertinent quantities from the inversions are displayed in a graph (Figure 7). The ordinate and the abscissa are the square roots of the two vector products in the cost function and are called the root mean square (rms) residual and rms roughness, respectively. The curve, which is called a trade-off curve, shows the rms residual and rms roughness that are obtained when the cost function is minimized with different values of λ. The magnitudes of the numbers are not important because all physical quantities — time, distances, and velocities — have been normalized; rather, the shape of the curve is important. For large values of λ (i.e., $1.\times10^{-3}$ to $3.\times10^{-2}$), a small increase in the rms roughness results in a large decrease in the rms residual — essentially, more information is being extracted from the data. At the other extreme, for small values of λ (i.e., $1.\times10^{-5}$ to $1.\times10^{-6}$), a large increase in the rms roughness results in a small decrease in the rms residual — essentially, the velocities on the grid are being adjusted to fit the noise in the data. The desired solution is between these two extremes, near the bend in the curve. Here, the misfits between the observed and predicted travel times are relatively small and the model is not too complicated. I have found that solutions near this knee are almost always geologically reasonable.

5. RESULTS

5.1 Well-to-Well Geometry, Saturated Zone

Sources and receivers were situated in wells MSB-3C and MSB-3B to probe completely the saturated zone in between the wells (Figure 1b), but only a subset of the data were used to compute the tomogram. The data collected near the water table were omitted because they had low amplitudes, which may have been caused by wave interference — a wave is probably being reflected from the top of the capillary fringe. The data from the lowest elevations in well MSB-3B were omitted because the waves were more dispersed than those collected at the higher elevations. (More dispersion occurred because the propagation distance was greater.) Even after this editing, plenty of data for the tomography remained, and the amount can be assessed by viewing the rays (Figure 6a).

The velocities for the region covered by the rays are displayed in the tomogram (Figure 8), and the location of this tomogram relative to the wells, ground surface, and water table is shown in Figure 1b.The left and right edges of the tomogram are at wells MSB-3C and MSB-3B, respectively, in which the sources and receivers were located; the top and

bottom edges are delineated by the rays at the top and bottom. The estimated velocities vary between 5344 and 5715 ft/s (1629 and 1742 m/s); this range is typical of saturated sediments at many locations (see e.g., Nur and Wang, 1989, chapter 2) including Savannah River Site (Hasbrouck, 1995). The reliability and non-uniqueness of these estimates can be determined qualitatively from the ray diagram (Figure 6a): at a given point, the greater the density and the angular coverage of the rays, the greater the reliability and the uniqueness of the estimated velocity (Bregman et al., 1989). Applying this rule, the velocities are reliable almost everywhere except at the top and bottom edges. (n. b., Although quantitative methods exist to compute the reliability and non-uniqueness (Aki and Richards, 1980, p. 686-689), they are never used in practice because they require too much computation.)

To interpret the tomogram, it will be analyzed in conjunction with three other types of data. The first are radar scans. The transmitting antenna was in well MSB-3C, the receiving antenna in MSB-3B at the same elevation. The significant characteristic to be observed in each scan is the amplitude of the wave, which is determined principally by its attenuation as it propagates between the antennas. Because the attenuation is much less in sands than in clays (Davis and Annan, 1989), high amplitude waves will be associated with sandy layers; either low amplitude waves or no detectable waves with clayey layers. The second are gamma ray measurements from geophysical logging in well MSB-3B. These measurements are probably detecting emissions from radioactive potassium in illite or from other radioactive minerals. Note that because kaolinite, which is the most prevalent clay near the M-Area basin (see Section 2), is not radioactive, the gamma ray measurements do not detect its presence. The last are percentages of clay-size particles that were estimated from samples of drill core from well MSB-3B. Clay-size particles are defined to be particles having a grain-size diameter less than 2.461×10^{-3} in (0.0625 mm) (Environmental Sciences Section, 1993), and consequently this measurement indicates the abundance of clays as well as any fine-grained particles like quartz.

At the top of the tomogram, from 215 to 212 ft, is a layer with a somewhat high velocity that is associated with high gamma ray measurements, moderate percentages of clay-size particles, and no detectable radar waves. This layer probably contains much clay. From 212 to 203 ft, the velocity is relatively low and is correlated with low gamma ray measurements, low percentages of clay-size particles, and high amplitude radar waves. This layer is probably sandy. Notice that the velocity within this layer varies indicating that it is heterogeneous — the heterogeneity is large enough (i.e., greater than approximately 3 ft) that it is detectable with seismic tomography. In the middle of the tomogram, from 203 to 198 ft, is a layer with a moderately high velocity that is associated with high gamma ray measurements, high percentages of clay-size particles, and no detectable radar waves. This layer probably contains a large amount of clay. From 198 to 194 ft is a layer with a moderately high velocity that is correlated with moderate to high gamma ray measurements, moderate percentages of clay-size particles, and radar waves with moderately high amplitudes. This layer is probably sandy but with very fine grains. From 194 to 183 ft is a heterogeneous layer with a high velocity; it is associated with relatively low gamma ray measurements and a mixture of low to moderate amounts of clay-size

particles. The correlation between seismic velocity and clay that exists above this interval does not seem to apply here. This discrepancy might be caused by the differences in the volumes being sampled and in their sizes — the tomogram pertains to the region between the wells and displays heterogeneity larger than approximately 3 ft, whereas the particle measurements pertain to the drill core from well MSB-3B and are average values for 1 ft sections. Below 183 ft, the velocities are low and are associated with low gamma ray measurements and low to moderate percentages of clay-size particles.

5.2 Well-to-Well Geometry, Unsaturated Zone

Sources and receivers were situated in wells MSB-3A and MSB-3B to probe completely the unsaturated zone between the wells (Figure 1b), but only a subset of the data were used to compute the tomogram. The data from sources and receivers near the ground surface and near the water table were omitted because the seismograms were too complex to pick. Near the surface, the complexity was probably caused by a wave that was refracted through a high velocity layer (see Section 5.3) and subsequently interfered with the direct wave. Near the water table, at least three phenomena might have caused the complexity. First, a wave probably refracted through the saturated zone. Second, when the tube wave in the source well hit the packer, additional waves were radiated into the ground. Finally, when the direct wave and the refracted wave hit the packer in the receiver well, tube waves were generated. After omitting these data, enough remained for a detailed analysis of a 50 ft interval in which the density of the rays is generally high (Figure 6b).

The velocities for the region covered by the rays are displayed in the tomogram (Figure 9), and the location of the tomogram relative to the wells, ground surface, and water table is shown in Figure 1b. The velocities vary between 1855 and 2899 ft/s (565 and 884 m/s); this range is typical of unsaturated sediments at other locations (see e. g., Press, 1966, p. 204) including Savannah River Site (Hasbrouck, 1995). Judging from the ray diagram (Figure 6b), the only locations where the estimated velocities might be unreliable are at the top and bottom edges and near 313 ft on the right hand side.

To interpret the tomogram, the gamma ray measurements, the percentages of clay-size particles, and amplitudes of the radar waves will be used as they were for the saturated zone. However, additional information about the geology may be extracted from the time travel of the radar wave. For electromagnetic wave propagation at the frequencies used for radar, a good approximation is that the velocity is inversely proportional to the square root of the real part of the dielectric permittivity (Stratton, 1941, p. 277). If most pores are filled with water, which has a high permittivity, then the permittivity of the sediment on the scale of a wave length will tend to be high, and the travel time high. Conversely, if most pores are filled with air, which has a low permittivity, then the permittivity of the sediment on the scale of a wave length will tend to be low, and the travel time low. In other words, the travel time in clayey sediments will be higher than that in sandy sediments because the partial saturation in the former is higher.

The geology may be divided into four sections. In the lowest, which extends from 280 to 290 ft, the seismic velocity is low to moderate, the amplitudes of the radar waves are high, their travel times are small, and the gamma ray measurements are moderate. Even though the percentages of clay-size particles are moderate, this section probably contains mostly sand. The next section, which extends from 290 to 319 ft, contains several layers that will be grouped together now and will be described separately later. The seismic velocities are moderate to high, the amplitudes of the radar waves are usually low to moderate, their travel times are large, and the gamma ray measurements and the percentages of clay-size particles are moderate to high. This section is probably clayey. In the next section, which extends from 319 to 328 ft, the seismic velocities are low, the amplitudes of the radar waves are high, their travel times are small and, the gamma ray measurements are somewhat low. The percentages of clay-size particles are either very small or zero. This section is probably sandy. In the top section, which is only about 2 ft thick, the seismic velocities are moderately high, and the amplitude of the radar wave is very low. Although the percentages of clay-size particles are zero, this section is probably clayey.

The thick section from 290 to 319 ft may be divided into three layers. In the lowest, from 290 to approximately 302 ft, the seismic velocities are high. Here most of the radar waves have low amplitudes, and the travel times are large. The gamma ray measurements and the percentages of clay-size particles are moderate to high. This layer is probably very clayey. The interpretation of the upper layer, from 311 to 319 ft, is similar. In the middle layer, from 302 ft to 311 ft, the seismic velocity is generally moderate. If an average velocity for each elevation were computed by summing the velocities in a horizontal direction (which happens to be the path of the radar wave), then this average would increase from bottom to top. This change can be correlated with changes in the radar waves: the amplitudes increase and the travel times decrease from bottom to top. Nothing significant is observed in either the gamma ray measurements or the percentages of clay-size particles. In this layer, the amount of clay is probably greatest at the bottom and decreases towards the top.

5.3 Surface-to-Well Geometry, Unsaturated Zone

Data were collected from sources located close to and far from well MSB-3B to thoroughly probe the unsaturated zone. However, the latter could not be included in the processing for two reasons. First, the direct waves were obscured by waves refracted through the saturated zone. Second, the direct waves had low amplitudes because the sources radiated little energy laterally (i.e., toward the hydrophone array) (White, 1983, p. 209) and because the waves, which propagated long distances, were severely attenuated. Nonetheless, the ray coverage from sources close to the well was sufficient to thoroughly sample the ground.

The top edge of the tomogram (Figure 10) corresponds to the surface of the ground, and the sides to the rays farthest from the well (Figure 6c). The location of the tomogram relative to the wells, ground surface, and water table is shown in Figure 1b. From 250 to 330 ft the velocities vary between 2116 and approximately 3000 ft/s (645 and 914 m/s); this range is typical for unconsolidated, partially saturated sediments. Above 330 ft, the

velocities are unusually high. From approximately 300 ft to the ground surface, the density and the angular coverage of the rays are moderately high (Figure 6c), and consequently the estimated velocities are reliable. Below approximately 300 ft the angular coverage is poor, and so the estimated velocities are only moderately reliable.

Unlike the interpretations of the other tomograms (see Sections 5.1 and 5.2) radar data will not be used here because acquiring radar data in a similar geometry is not feasible. (There are two reasons: the electromagnetic waves would have to propagate through many clay layers that would severely attenuate the waves, and the antennas would be oriented with the minimal coupling.) The tomogram may be divided into three intervals. Between 250 and 271 ft, the estimated velocities are moderately high, and the percentages of clay-sized particles and the gamma ray measurements are intermittently high. This interval may be clayey. Between 271 and 330 ft, the velocities are generally low, and the percentages of clay-size particles and the gamma ray measurements are moderate. No significant correlation between the tomogram and the well data is evident. Above 330 ft, the velocities are high, and this anomaly may be due to soil that was compacted while the cap for the basin was being constructed.

5.4 Discussion

The problems with the data — the noise on receiver number 7, the mixing of the channels, and the irregular trigger — increased the complexity of and the time required for the processing. However, these problems probably did not diminish the quality of the tomograms significantly because the data have so much redundancy. If seismic tomography were to be used again at SRS, then clearly better equipment should be used.

For the interpretation of the tomograms (Sections 5.1 and 5.2), the *P*-wave velocities were compared qualitatively to the percentages of clay-size particles, the radar amplitudes, and the radar travel times. To better define the relations among these parameters, they were plotted. First, for the saturated and unsaturated zones the velocities at well MSB-3B from each tomogram were plotted against an average percentage of particles (Figures 11a and 11b, respectively). The averaging, which was over a 3 ft interval, was done to make the scales of measurement somewhat similar. If the data from 183 to 194 ft, which lies within the saturated zone, are excluded, then the remaining data indicate that the higher the percentage of clay-size particles, the higher the velocity. A hypothesis for this relation is that the clays have stiffened the sediment matrix, increasing the *P*-wave velocity. At least two mechanisms might cause such stiffening: Dispersed clays could be weakly cementing quartz grains together, a phenomenon observed by Seagull (1992) in the sediments at Savannah River Site. Alternatively, when the stratigraphy consists of distinct, thin layers of clays and sands, its average velocity will be higher than that of a single layer of pure sand (see e.g., White, 1983 , p. 49-55). Second, for the saturated zone, averaged *P*-wave velocities were plotted against amplitudes of the radar waves (Figure 12). Each average velocity is the arithmetic mean of the velocities in the tomogram along a (straight) line at the elevation of the radar antennas. Each amplitude is the root mean square of the values representing the radar scan within a window centered on the arriving wave.

Excluding the data for which the ray density is low (from 212 to 218 ft), the remaining data indicate that the higher the velocity, the lower the amplitude of the radar wave. The clays are probably stiffening the sediment matrix and attenuating the radar waves. For the unsaturated zone, the correlation between the velocities and amplitudes is relatively poor, and so a similar generalization could not be made. Finally, for the unsaturated zone, averaged *P*-wave velocities were plotted against the travel times of the radar waves (Figure 13). Each averaged velocity was computed as it was for Figure 12. The data indicate that the higher the seismic velocity, the higher the radar travel time. The clays are probably stiffening the sediment matrix and retaining water in the pores (see Section 5.2).

The estimated velocities for the saturated zone (Figure 8) are approximately double those for the unsaturated zone (Figure 9), regardless of the lithology. A similar phenomenon has been observed in laboratory experiments: At low confining pressures, the velocity of *P*-wave propagation in a partially saturated, unconsolidated sand is low but increases markedly as the saturation approaches 100% (Allen et al., 1980). At high confining pressures, the velocity increases in a similar manner (Elliot and Wiley, 1975; Domenico, 1977). Thus, the large increase in velocity between the unsaturated and saturated zones is probably caused by the degree of saturation.

Comparing the well-to-well tomogram from the unsaturated zone (Figure 9) to the surface-to-well tomogram (Figure 10) between 280 and 330 ft, the range in velocities is similar, but at any particular point the velocities do not match. To understand this discrepancy, the wave length in both experiments must be considered because over this distance a wave is affected by the average properties of the medium. For the well-to-well geometry, the shortest wave length was approximately 1.3 ft (0.40 m), whereas for the surface-to-well geometry, it was approximately 10 ft (3.0 m). Therefore, the scale of the measurement for the well-to-well geometry was much smaller than that for the surface-to-well geometry, and concomitantly the resolution is much better.

In some recent laboratory experiments (Geller and Myer, 1993), DNAPL in saturated, unconsolidated sediments was shown to diminish the velocity of *P*-wave propagation, and thus a pertinent question is whether the seismic method should be considered for characterization and monitoring of DNAPL remediation at SRS. The results of this feasibility study might be helpful in addressing this question. First, the direct detection of DNAPL will be considered. Assume that the lithology is known because it, as well as the pore fluids, can affect velocity and amplitude, and assume that the percentage of clay-size particles is a suitable indicator of lithology. Figures 11a and 11b indicate that for a given percentage (i.e., for a given lithology) the velocities can vary significantly, especially in the saturated zone. The problem is that these variations are as large as (or even larger than) what would be predicted for a typical increase in DNAPL concentration using Geller and Myer's results (i.e., velocity decreases 2 % as the DNAPL concentration increases from 0 % to 20 % and decreases 13 % as it increases from 20 % to 40 %). For this reason, the direct detection of DNAPL using the seismic method appears to be very difficult. Criticisms of this argument are that the scatter in Figures 11a and 11b would be significantly reduced if the velocities were more accurate, that better indicators of

lithology might exist, and that the results of Geller and Meyer's experiments, for which the frequencies were approximately 40 kHz and Freon 113 was used as the DNAPL, may not be applicable to the situation at SRS. Only more research could resolve these criticisms.

The second issue regarding the use of the seismic method in DNAPL remediation is mapping the layers from which DNAPL has been removed. (1) If a tomographic method were used, then the key to addressing this issue is the size of the Fresnel zone compared to the thickness of the sediments containing significant amounts of DNAPL (i.e., approximately 30 % of pore volume containing DNAPL). Assume that this thickness is about 1 ft (0.3 m), which might be slightly larger than what is believed to be typical at SRS (B. Looney, oral commun., 1995); assume that the wells are separated by 30 ft; and assume that the velocity is 5.5×10^3 ft/s (1.7×10^3 m/s), which is a suitable average for the saturated zone. Because the size of the heterogeneity that can be resolved is slightly less than the size of the Fresnel zone (Williamson and Worthington, 1993), assume that the Fresnel may be as large as 2 ft between the wells. For this situation, the frequencies must be as high as 11 kHz to resolve the layer. The problems are that at this time no sources exists to generate frequencies over approximately 7 kHz and that the components of the wave at high frequencies will be severely attenuated. (2) If a reflection method were used, then the key to mapping the layers from which DNAPL has been removed is observing reflected waves from those layers. In the surface-to-well configuration for the unsaturated zone (Figure 4), a weak reflected wave attributable to the velocity change between the unsaturated and saturated zones can be observed (receivers 1 to 6). The problem is that if a 200 % change in velocity (c.f., Figures 8 and 9) causes only a weak reflection, then a 15 % change due to DNAPL extraction would be undetectable. (This 15 % change was calculated using Geller and Myer's (1993) results: The velocity of *P*-wave propagation in an unconsolidated sand increases 15 % as the saturation of DNAPL decreases from 40 % to 0 %.)

6. SUMMARY AND RECOMMENDATIONS

The objectives that were established in the Introduction (Section 1) were accomplished for all three experiments that constituted the feasibility test. From these objectives, much was learned about the extent to which the site conditions affect seismic tomography.

In the unsaturated zone using the surface-to-well geometry, seismic waves could be generated and recorded indicating that the mechanical couplings between the source and the near-surface soil and between the grout and the sediments are good. However, the waves were highly attenuated and dispersed, compromising the assumptions inherent in the processing. Because the frequencies were low (i.e., below approximately 350 Hz), the resolution was approximately 10 ft. This distance is greater than the scale length of the heterogeneity in the vertical direction, and thus the tomogram could not be used to delineate the stratigraphy. Even with sources capable of generating somewhat higher frequencies, the resolution will not improve significantly. At Savannah River Site, surface-to-well seismic tomography using current technology is not a useful tool for mapping stratigraphy in the unsaturated zone. Nonetheless, processing methods using the full wave

field that are currently being proposed for research should have much better resolution, and with them stratigraphy probably could be mapped.

In the unsaturated zone using the well-to-well geometry, waves readily propagated between the wells indicating the mechanical coupling between the grout and the sediments is strong. Like the experiment with the surface-to-well geometry, the waves were highly attenuated and dispersed. Nonetheless, over the short propagation distances (i.e., 15 to 25 ft) enough components at high frequencies (i.e., up to 1 kHz) were transmitted that the size of the smallest heterogeneity that could be detected was approximately 3 ft. This distance is small enough that significant details in the stratigraphy could be delineated. The features in the tomogram correlate with independent information about the geology: the velocities are well correlated with the percentages of clay-size particles and with the travel times of the radar waves, and sometimes they are correlated with the amplitudes of the radar waves. Using current technology, seismic tomography between closely spaced wells (i.e., less than approximately 20 ft) can be used to map stratigraphy. If the wells are widely spaced, then attenuation and dispersion will be more severe, and so processing methods that use the full wave field will be necessary. Tomography near the water table will be difficult because the direct wave may be obscured by waves refracted through the saturated zone and by waves scattered from the packers.

In the saturated zone using the well-to-well geometry, the amplitudes of the recorded waves were very high indicating that the mechanical coupling between the grout and the sediments is good. Unlike the experiments in the unsaturated zone, attenuation and dispersion were only moderate, and so waves with frequencies as high as 2 kHz propagated twice as far. The size of the smallest heterogeneity that could be resolved in the tomogram was approximately 3 ft, which was small enough that details in the stratigraphy could be identified. The features in the tomogram correlate with independent information about the geology: the velocities are moderately well correlated with the percentages of clay-size particles (except in one interval) and with the amplitudes of the radar waves. Using current technology, seismic tomography can be a useful tool for high resolution mapping of stratigraphy in the saturated zone and probably can be used in wells separated by as much as 50 ft.

Of the three geometries considered in this feasibility study, well-to-well tomography in the saturated zone seems to be the best suited to mapping stratigraphy, and it should be considered when other, less expensive methods like cone penetrometer are unsuitable. In addition to helping hydrologists design the remediation program, this stratigraphic information is crucial for processing and interpreting borehole radar data because geophysicists will used it to separate the effects on the radar waves due to stratigraphy from those due to pore fluids. In this way the inherent ambiguity in the interpretation of borehole radar data ought to be diminished, and the monitoring of DNAPL remediation improved.

7. ACKNOWLEDGEMENTS

I wish to thank D. C. Muller, who helped with the data collection, B. Pemberton, who organized all of the field support, and C. Eddy-Dilek, who coordinated the field work and provided the logging data. This work was sponsored by the Department of Energy under Interagency Agreement DE-AI09-91SR18222.

8. REFERENCES

Allen, N. F., Richart, F. E., Jr., Woods, R. D., 1980, Fluid wave propagation in saturated and nearly saturated sands: Journal of the Geotechnical Engineering Division, American Society of Civil Engineers, vol. 106, p. 235-254.

Aki, K., and Richards, P. G., 1980, Quantitative seismology, Theory and methods: San Francisco, W. H. Freeman and Co., 932 p.

Barry K. M., Cavers, D. A., Kneale, C. W., 1980, Recommended standards for digital tape formats *in* Digital tape standards: Tulsa, Oklahoma, Society of Exploration Geophysicists, p. 22-30.

Block, L. V., 1991, Joint hypocenter-velocity inversion of local earthquake arrival time data in two geothermal fields, PhD thesis, Massachusetts Institute of Technology, 448 p.

Block, L. V., Cheng, C. H., Fehler, M. C., and Phillips, W. S., 1994, Seismic imaging using microearthquakes induced by hydraulic fracturing: Geophysics, v. 59, p. 102-112.

Bregman, N. D., Bailey, R. C., and Chapman, C. H., Ghosts in tomography: The effects of poor angular coverage in 2-D seismic traveltime inversion: Canadian Journal of Exploration Geophysics, vol. 25, p. 7-27.

Davis, J. L., and Annan, A. P., 1989, Ground penetrating radar for high-resolution mapping of soil and rock stratigraphy: Geophysical Prospecting, vol. 37, p. 531-551.

DiStefano, M., 1989, Soil characterization at the Savannah River plant: Mineralogy, Technical Services Report No. 1809-005-011-1-89, Conoco Exploration Research & Services, available from Environmental Sciences Section, Westinghouse Savannah River Company, Aiken, SC 29808

Domenico, S. N., 1977, Elastic properties of unconsolidated porous sand reserviors: Geophysics, vol. 42, p. 1339-1368.

Eddy-Dilek, C. A., Looney, B. B., Hazen, T. C., Nichols, R. L., Fliermans, C. B., Parker, W. H., Dougherty, J. M., Kaback, D. S., and Simmons, J. L., 1993, Post-test evaluation of the geology, geochemistry, microbiology, and hydrology of the *in situ* air stripping demonstration site at the Savannah River Site, Report No. WSRC-TR-93-369, Westinghouse Savannah River Company, Aiken, SC 29808

Elliot, S. E., and Wiley, B. F., 1975, Compressional velocities of partially saturated, unconsolidated sands: Geophysics, vol. 40, p. 949-954.

Environmental Sciences Section, 1993, Microscopic examination of sediment cores, Manual WSRC-L14.1, Procedure 2-15, Rev.2, available from Environmental Sciences Section, Westinghouse Savannah River Company, Aiken, SC 29808

Everest Geotech Company, date unknown, Integrated model of the geologic system at Savannah River plant, Aiken, South Carolina, available from Environmental Sciences Section, Westinghouse Savannah River Company, Aiken, SC 29808

Geller, J. T., and Myer, L. R., 1993, Seismic imaging of organic liquid contaminants in unconsolidated media, EOS Transactions, American Geophysical Union, vol 74., p. 318.

Hasbrouck, W. P., 1995, Surface-to-hole seismic velocity survey at the borehole BGO46B, F area, DOE Savannah River Site, South Carolina: U. S. Geological Survey Administrative Report, 130 p.

Horton, R. J., 1995, X-ray diffraction studies of selected core samples from A/M area, Savannah River Site, South Carolina: U. S. Geological Survey Open File Report, *in preparation.*

Jordan, J. E., Looney, B. B., Rossabi, J., Bergren, C. L., 1993, Savannah River Site DNAPL Technical Program Plan, Report No. WSRC-TR-93-606, Westinghouse Savannah River Company, Aiken, SC 29808

Lines, L. R., and Treitel, S., 1984, A review of least-squares inversion and its application to geophysical problems: Geophysical Prospecting, vol. 32, p. 159-186.

Nur, A. M., Wang, Z., *eds.*, 1989, Seismic and acoustic velocities in reservior rocks, Volume 1, Experimental studies: Society of Exploration Geophysicists, Tulsa, Oklahoma, 405 p.

Phillips, W. S., and Fehler, M. C., 1991, Traveltime tomography: A comparison of popular methods: Geophysics, v. 56, p. 1639-1649.

Press, F., 1966, Seismic velocites, *in* Clark, S. P., Jr., ed., Handbook of Physical Constants: Geological Society of America Memoir 97, p. 195-218.

Oyo Corporation, 1986, Operation Manual, Model - 3792, Drift Log Measuring Module, available from Oyo Geospace, Engineering Geophysics Div., W. Gulf Bank, Suite 10, Houstion, TX 77040.

Oyo Corporation, 1991, Operation Manual, Model - 11122, McSEIS 170f, available from Oyo Geospace, Engineering Geophysics Div., W. Gulf Bank, Suite 10, Houstion, TX 77040.

Oyo Corporation, 1993, Operation Manual, Model - 1394/1395, OWS, available from Oyo Geospace, Engineering Geophysics Div., W. Gulf Bank, Suite 10, Houstion, TX 77040.

Scales, J. A., and Gersztenkorn, A., 1988, Robust methods in inverse theory: Inverse Problems, vol. 4, p. 1071-1091.

Scales, J. A., Gersztenkorn, A., and Treitel, S., 1988, Fast l_p solution of large, sparse linear systems: Application to seismic travel time tomography: Journal of Computational Physics, v. 75, p. 314-333.

Seagull, M. P., 1992, Clay-size mineralogic studies of selected samples from the Upland unit, Tobacco Road sands, Dry Branch formation, and Santee formation, South Carolina, *in* Sedimentology and stratigraphy of the Upland Unit, Progress Report, December 2, 1992, available from University of South Carolina, Department of Geological Sciences.

Stratton, J. A., 1941, Electromagnetic theory: New York, McGraw-Hill Inc., 615 p.

Um, J., and Thurber, C., 1987, A fast algorithm for two-point seismic ray tracing: Bulletin of the Seismological Society of America, v. 77, p. 972-986.

Westinghouse Savannah River Company, 1992, Assessing DNAPL contamination, A/M-area, Savannah River Site: Phase I results, Report No. WSRC-RP-92-1302, available from Environmental Sciences Section, Westinghouse Savannah River Company, Aiken, SC 29808

White, J. E., 1983, Underground sound, Application of seismic waves: Elsevier Science Publishers B. V., Amsterdam, 253 p.

Williamson, P. R., and Worthington, M. H., 1993, Resolution limits in ray tomography due to wave behavior: Numerical experiments: Geophysics, v. 58, p. 727-735.

Yilmaz, Ö., 1987, Seismic data processing: Tulsa, Oklahoma, Society of Exploration Geophysicists, 526 p.

Table 1. Location of wells on the north side of the M-Area basin. The locations are specified in the Savannah River Site coordinate grid.

Well Name	North Coordinate (ft)	East Coordinate (ft)	Elevation (ft)
MSB 3A	102190.06	48553.86	358.70
MSB 3B	102191.68	48567.43	358.92
MSB 3C	102189.66	48537.93	358.75
MSB 3D	102188.76	48524.58	358.80
MSB 22	102195.23	48510.10	358.51
MSB 58D	102200.79	48693.55	355.92

Table 2. Location of shots used for the surface-to-well geometry. The locations are specified in the Savannah River Site coordinate grid.

Shot Name	North Coordinate (ft)	East Coordinate (ft)	Elevation (ft)
S-12	102183.66	48537.61	358.35
S-14	102184.10	48544.18	358.38
S-16	102184.55	48550.66	358.19
S-18	102185.05	48557.26	358.25
S-20	102185.68	48563.80	358.27
S-22	102186.10	48570.38	358.38
S-24	102186.64	48576.89	358.22
S-26	102187.25	48583.32	358.31
S-28	102187.76	48589.84	358.35
S-30	102188.08	48596.38	358.41
S-32	102188.71	48603.00	358.35
S-34	102189.14	48609.56	358.38
S-36	102189.42	48616.10	358.26
S-38	102190.07	48622.59	357.92
S-40	102190.48	48629.17	357.63
S-42	102191.00	48635.58	357.53
S-44	102191.31	48642.17	357.39
S-46	102191.92	48648.73	357.21
S-48	102192.39	48665.30	356.99
S-50	102192.97	48661.75	356.83
S-52	102193.07	48668.38	356.66
S-54	102193.66	48674.85	356.29
S-56	102194.17	48681.34	355.90
S-58	102194.58	48687.77	355.78

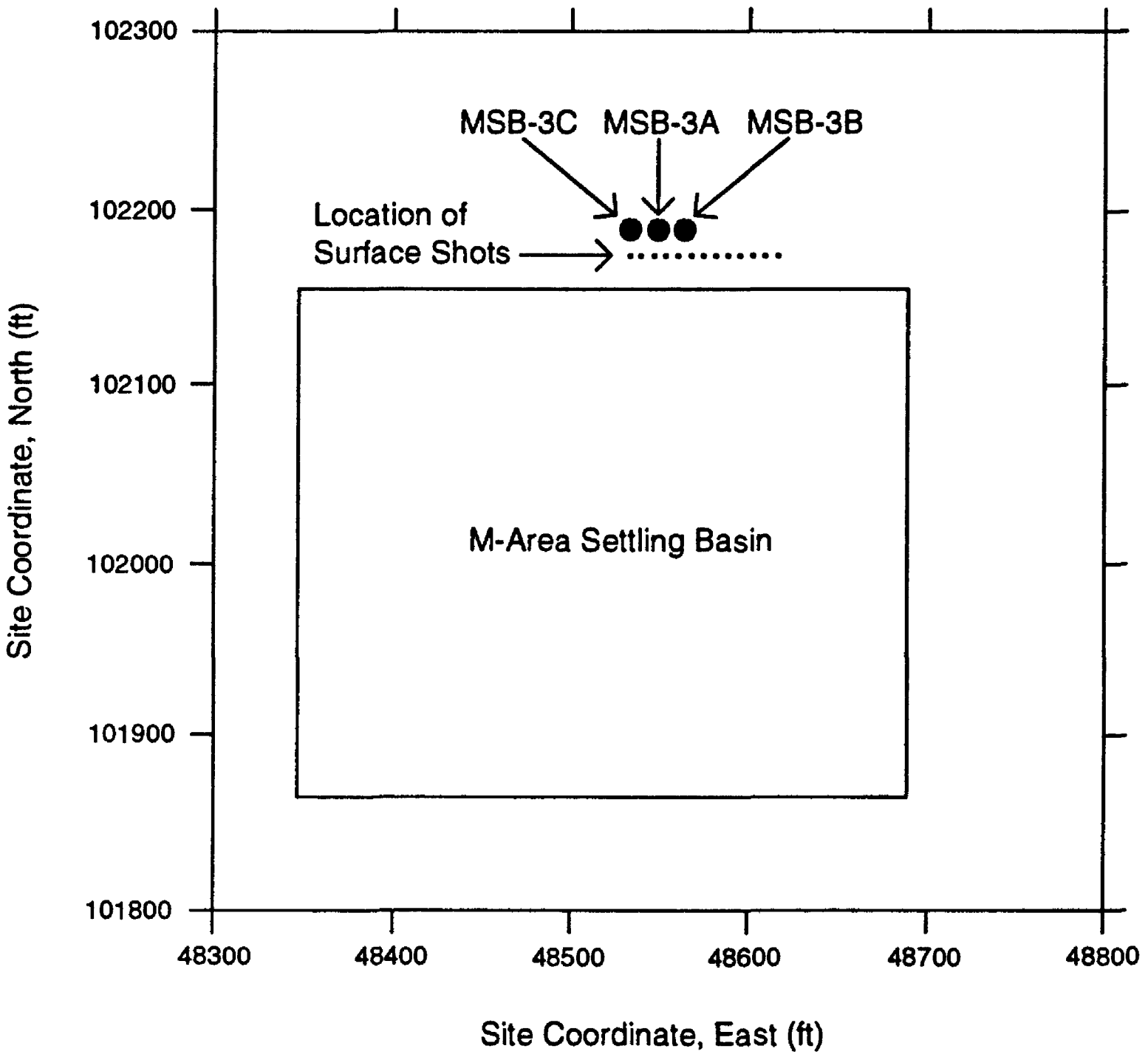

(a)

Figure 1. (a) Plan view of wells and shot locations used for the seismic tomography. (b) Vertical cross section through the line of surface shots shown in (a). The red, green, and blue polygons outline the regions for which tomograms were computed. Cross section is to scale.

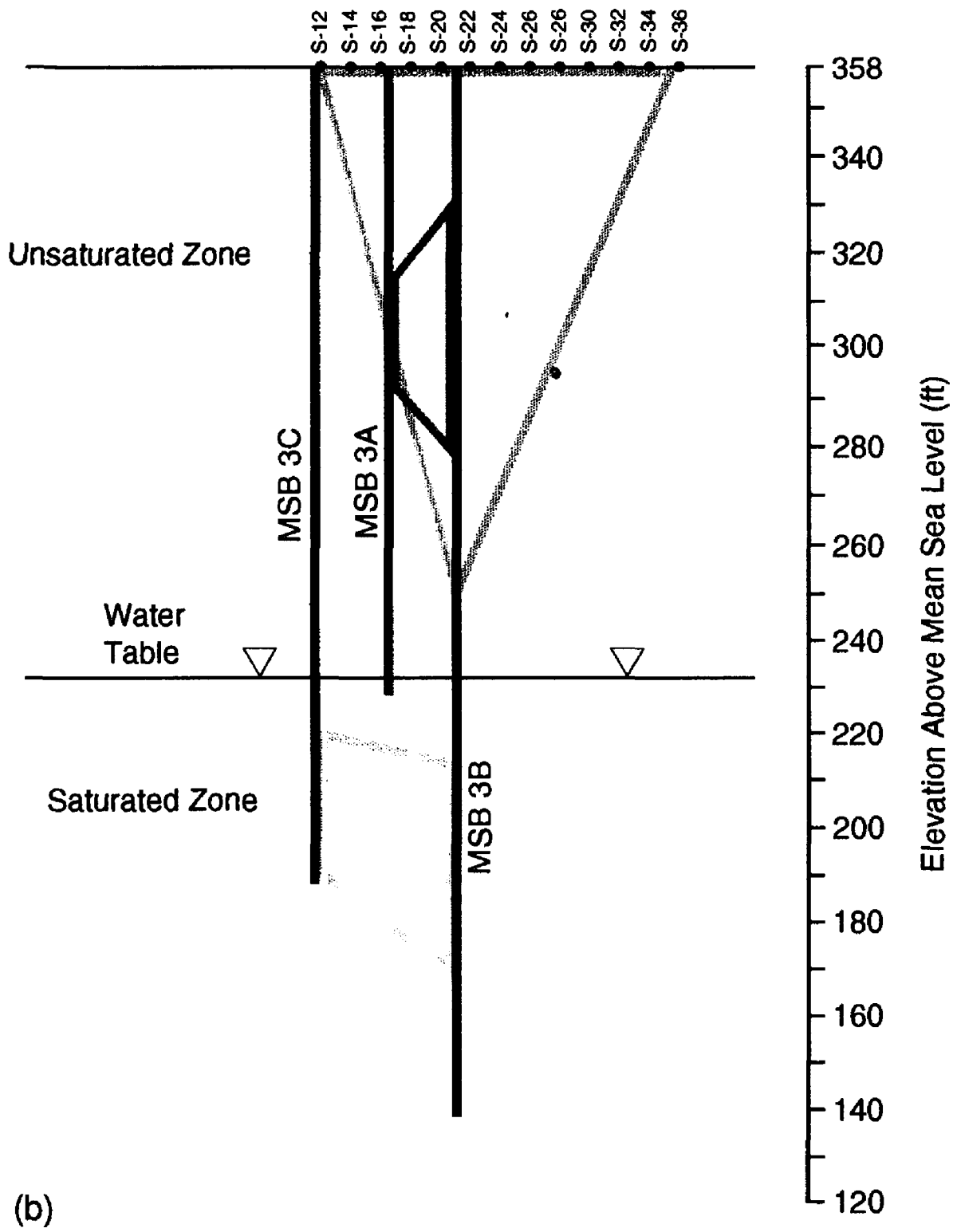

(b)

Figure 1. continued.

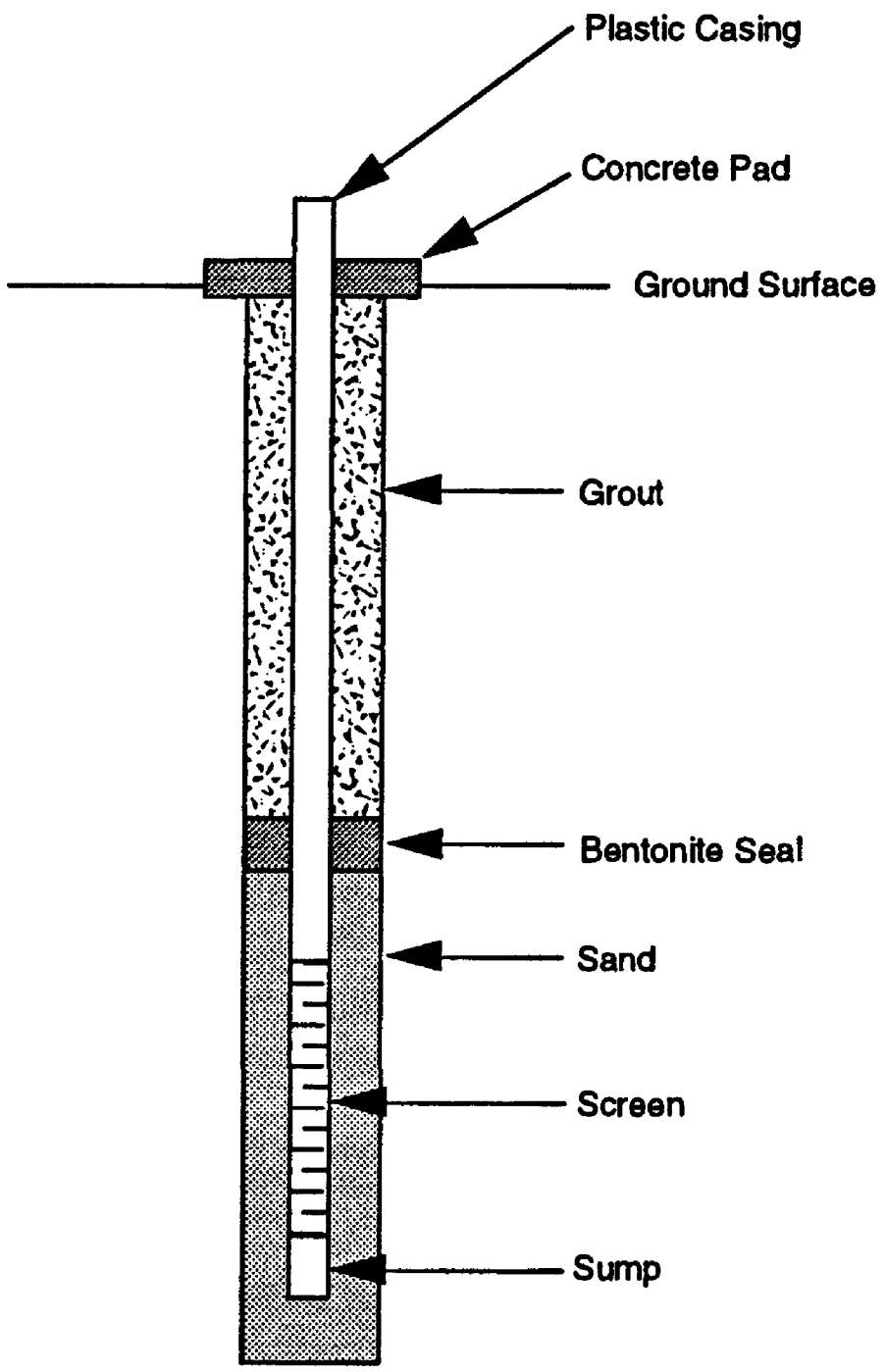

Figure 2. Typical construction of a monitor well. This diagram is not to scale.

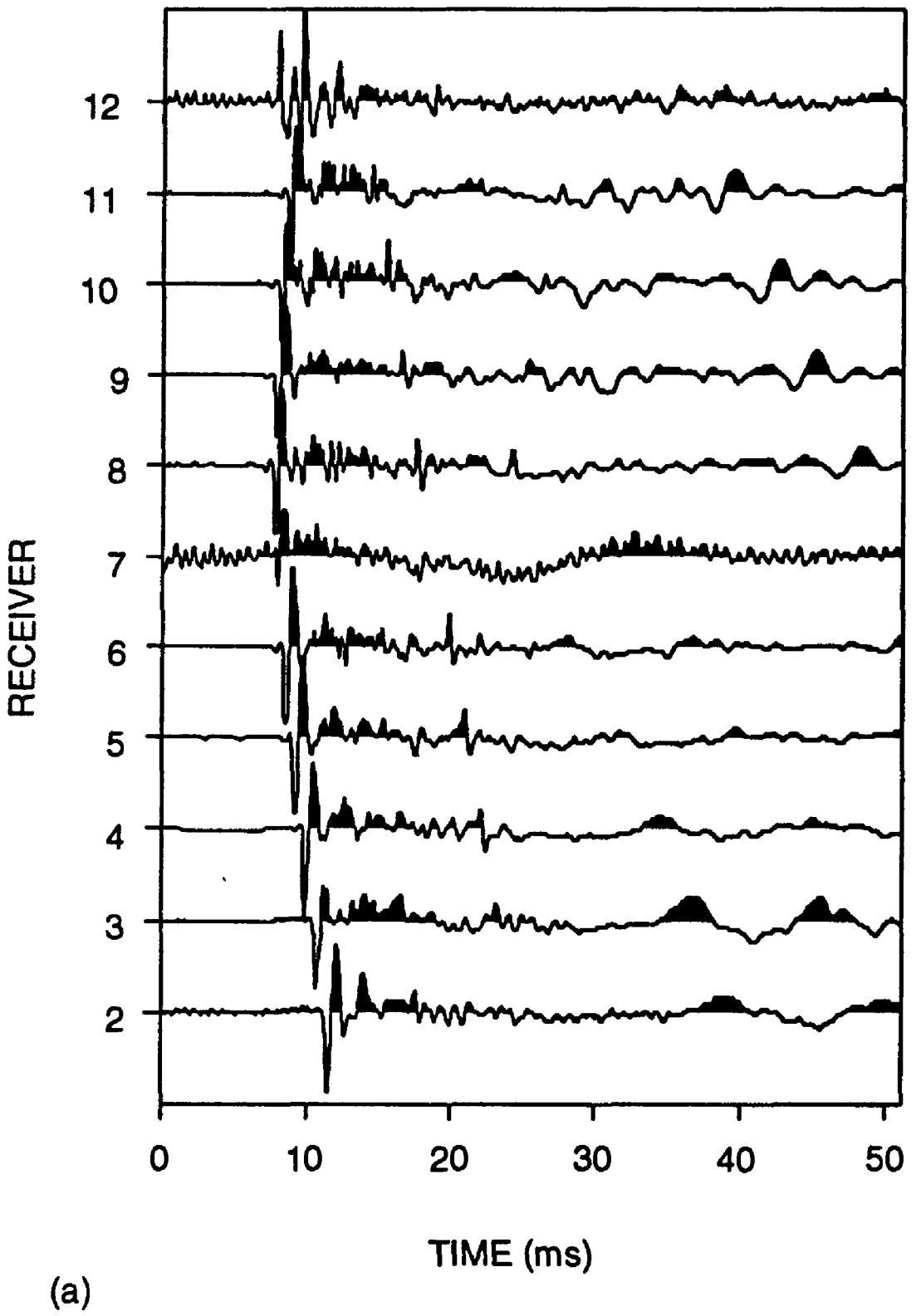

Figure 3. Common shot gathers (well-to-well geometry) from the (a) saturated and (b) unsaturated zones. For the saturated zone, the source was in well MSB-3C at an elevation of 190.2 ft, the receivers in MSB-3B at elevations between 148.7 and 214.4 ft. For the unsaturated zone, the source was in well MSB-3A at an elevation of 306.5 ft, the receivers in MSB-3B at elevations between 283.1 and 348.7 ft. The seismogram for receiver 1 is missing because this channel was used to record the trigger. The reasons for the noise on receiver number 7 and for the mixed seismograms are explained in the text.

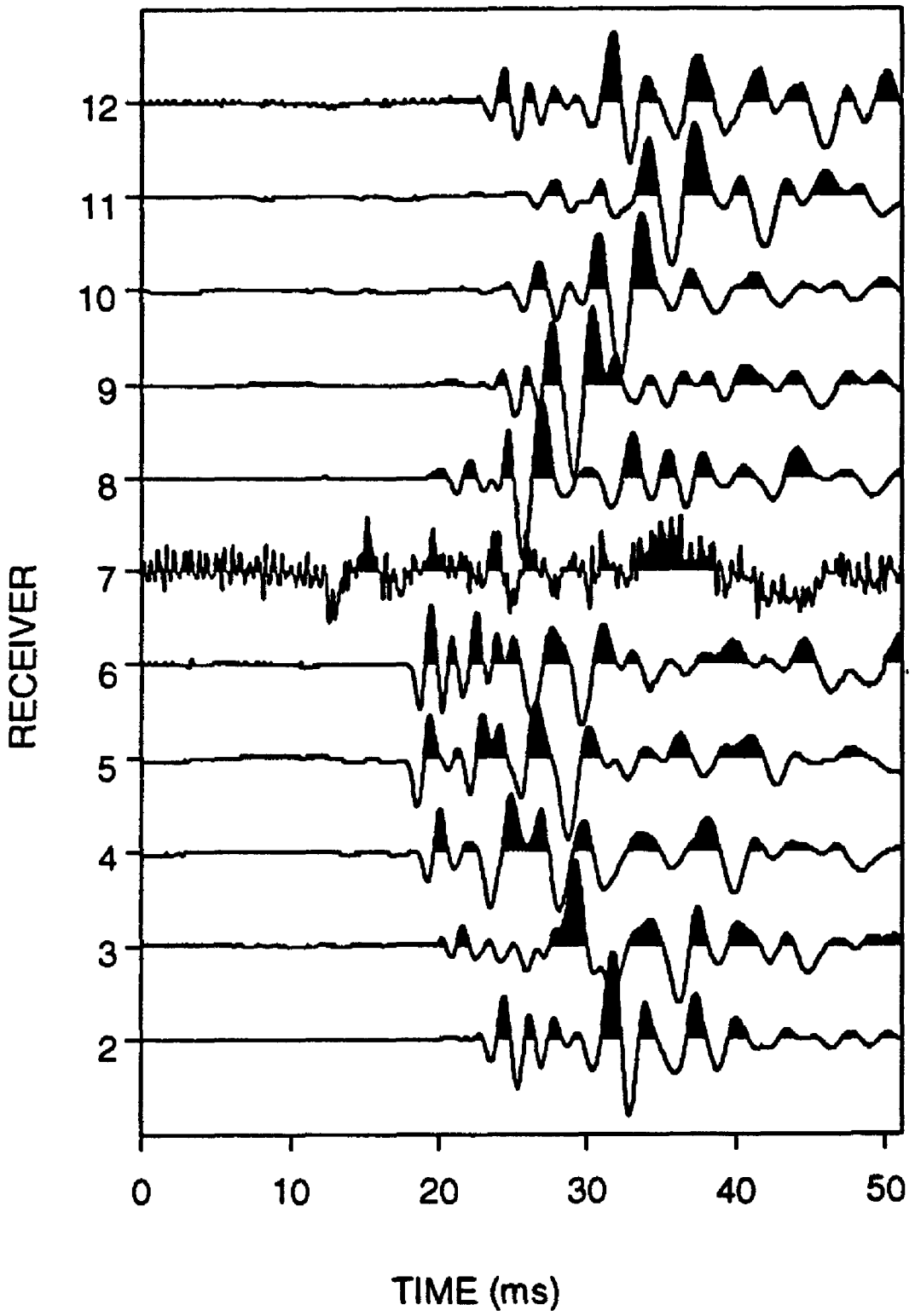

(b)

Figure 3. continued.

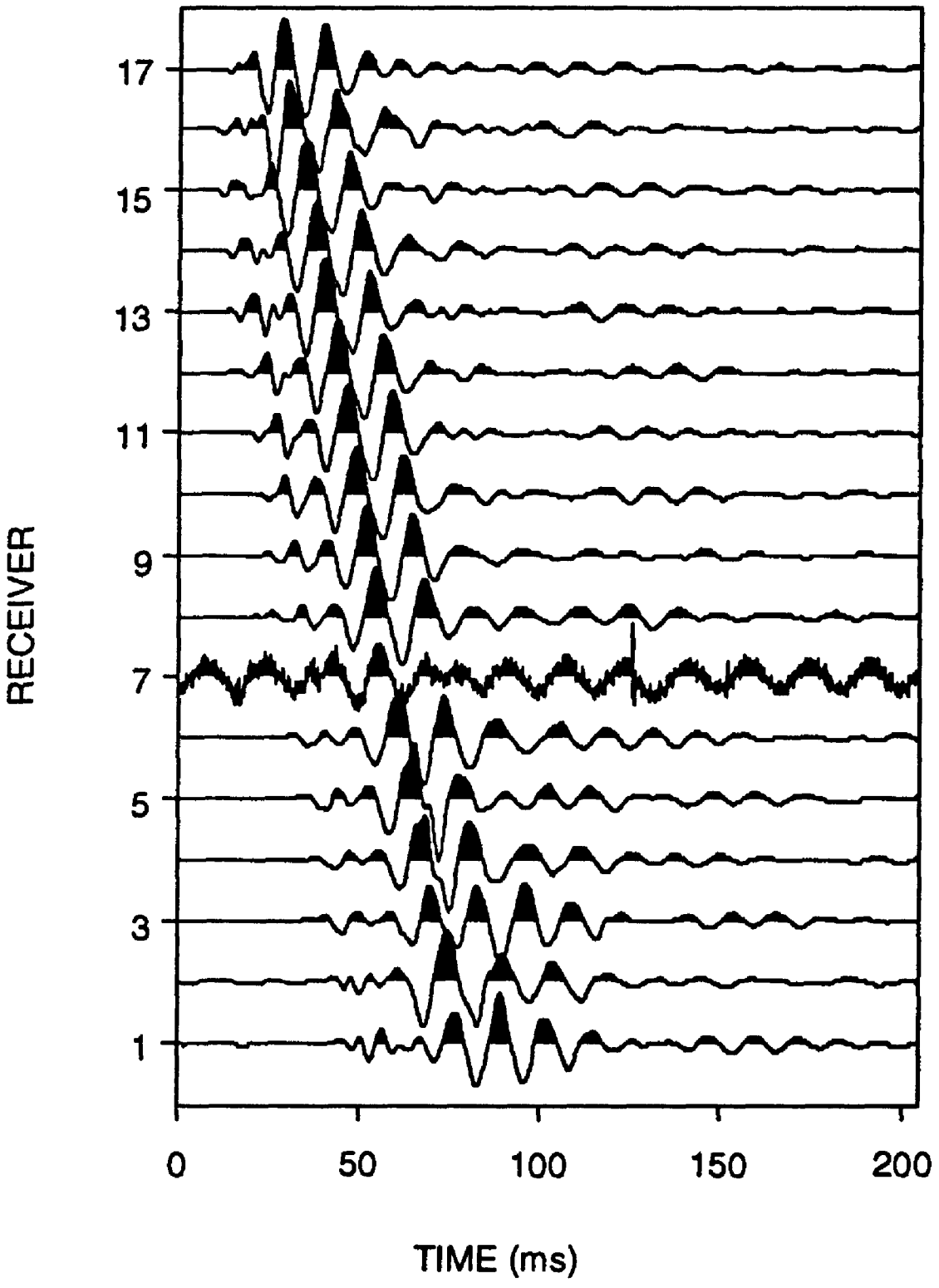

Figure 4. A common shot gather (surface-to-well geometry) from the unsaturated zone. The source was on the surface at shot location S-26 (Figure 1b), and the receivers were in well MSB-3B at elevations between 250.9 and 355.9 ft. The reason for the noise on receiver number 7 is explained in the text.

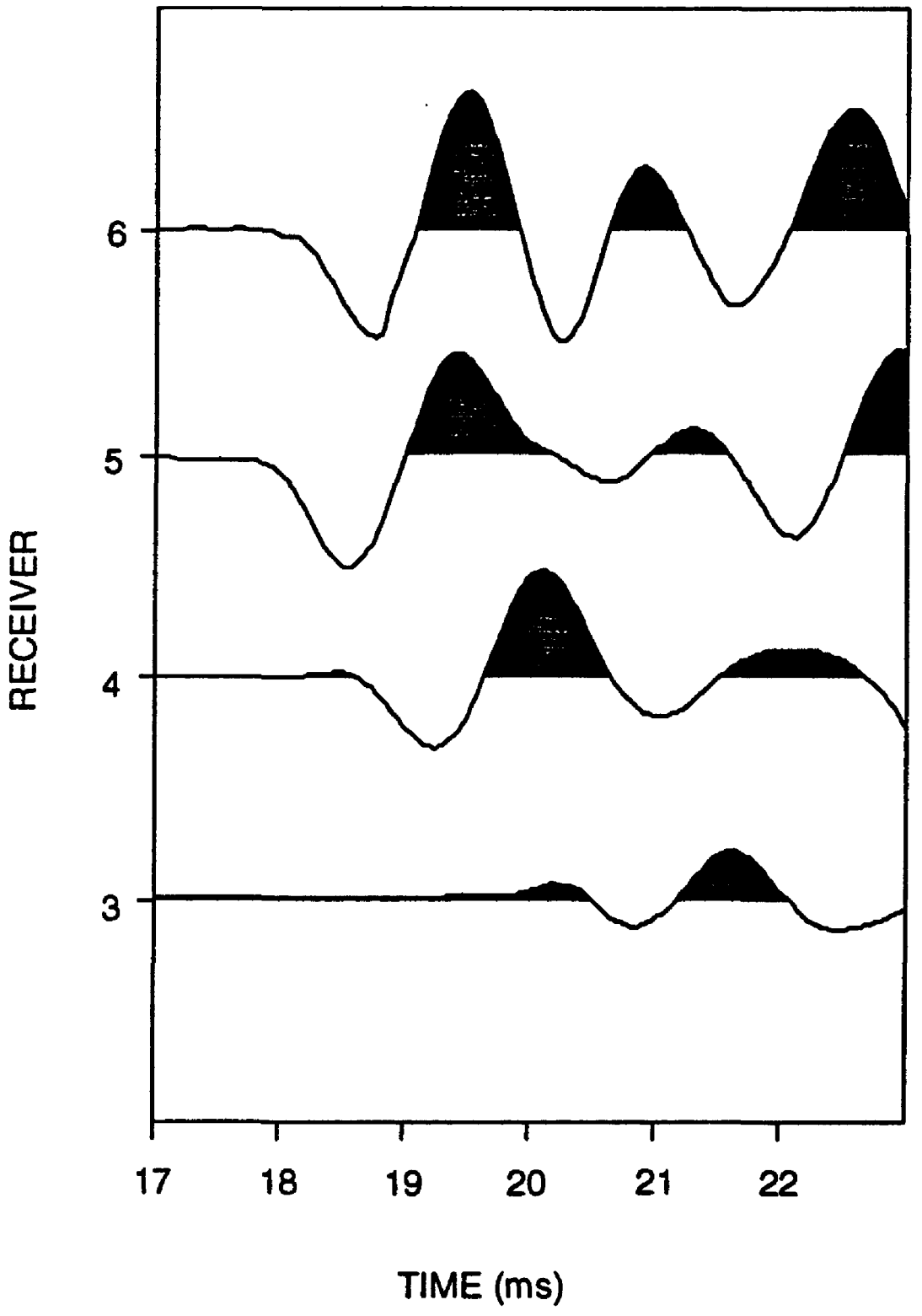

Figure 5. Close-up view of seismograms showing the effects of dispersion. These seismograms are from a common shot gather collected in the well-to-well geometry from the unsaturated zone (Figure 3b).

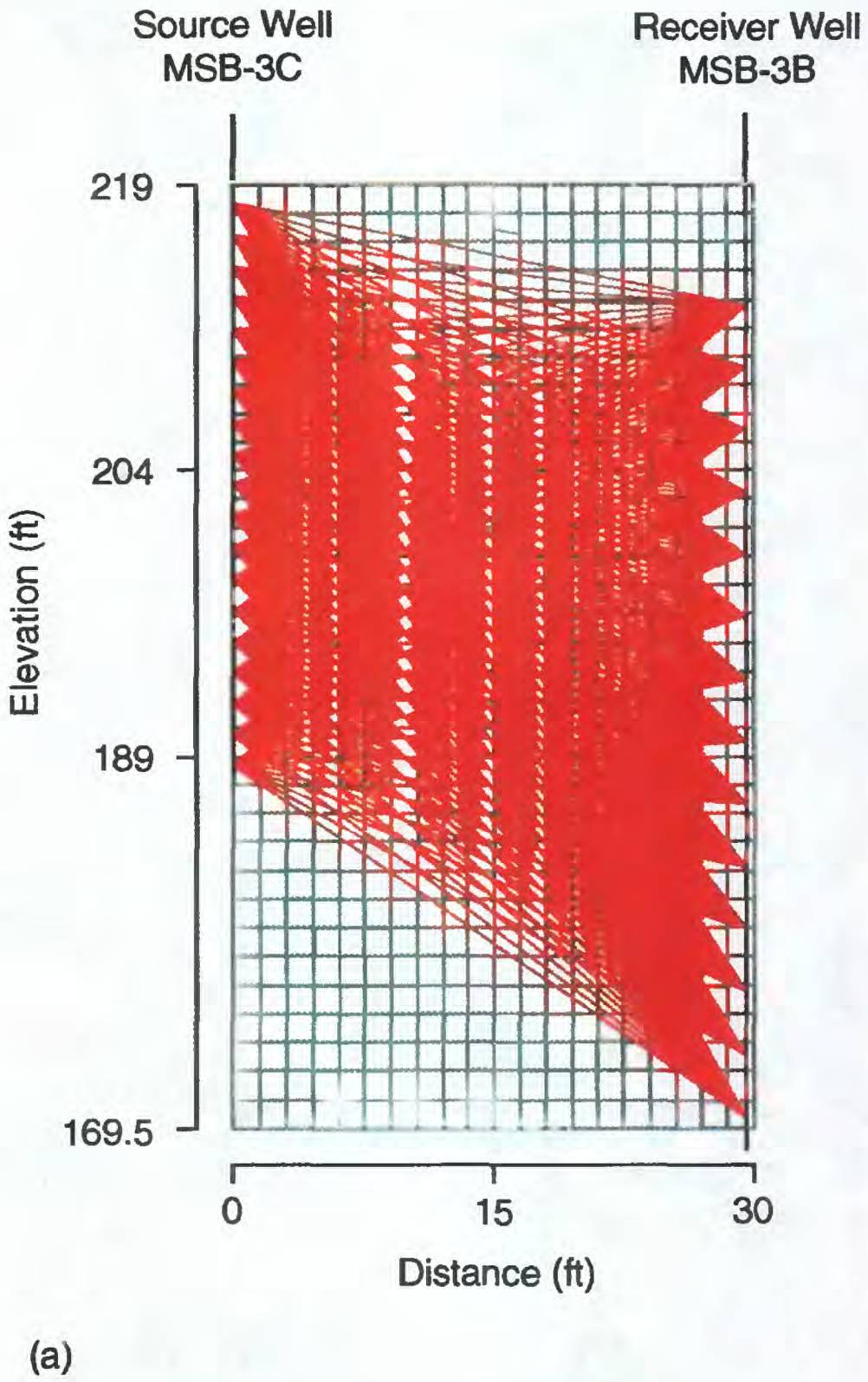

Figure 6. Grid used for (a) the well-to-well tomography in the saturated zone, (b) the well-to-well tomography in the unsaturated zone, and (c) the surface-to-well tomography in the unsaturated zone. Each ray represents one travel time pick, and the sources and the receivers were located where the rays intersect the wells. The regions containing the rays match those for which tomograms were computed, and their locations are shown in Figure 1b.

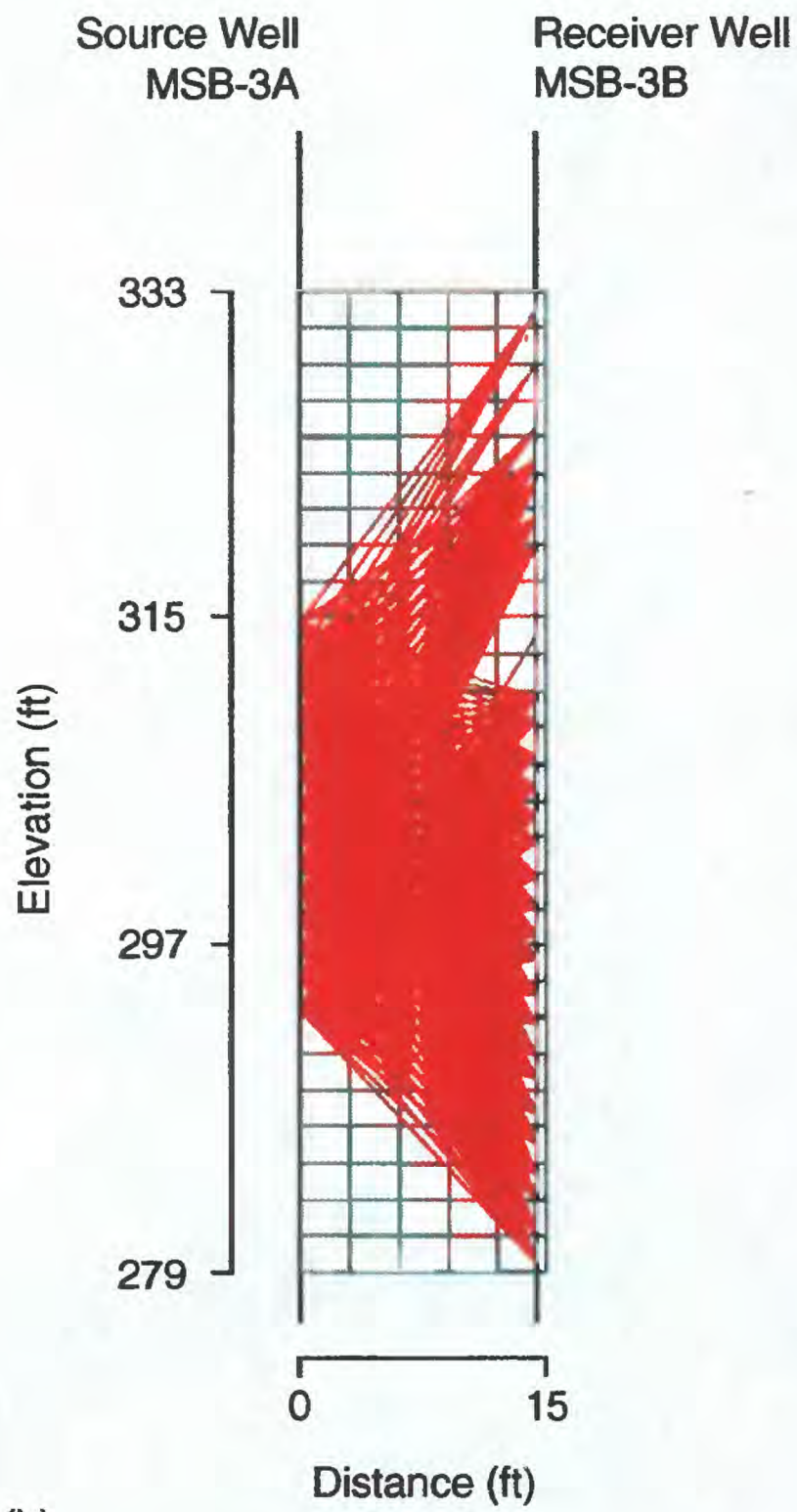

(b)

Figure 6. continued.

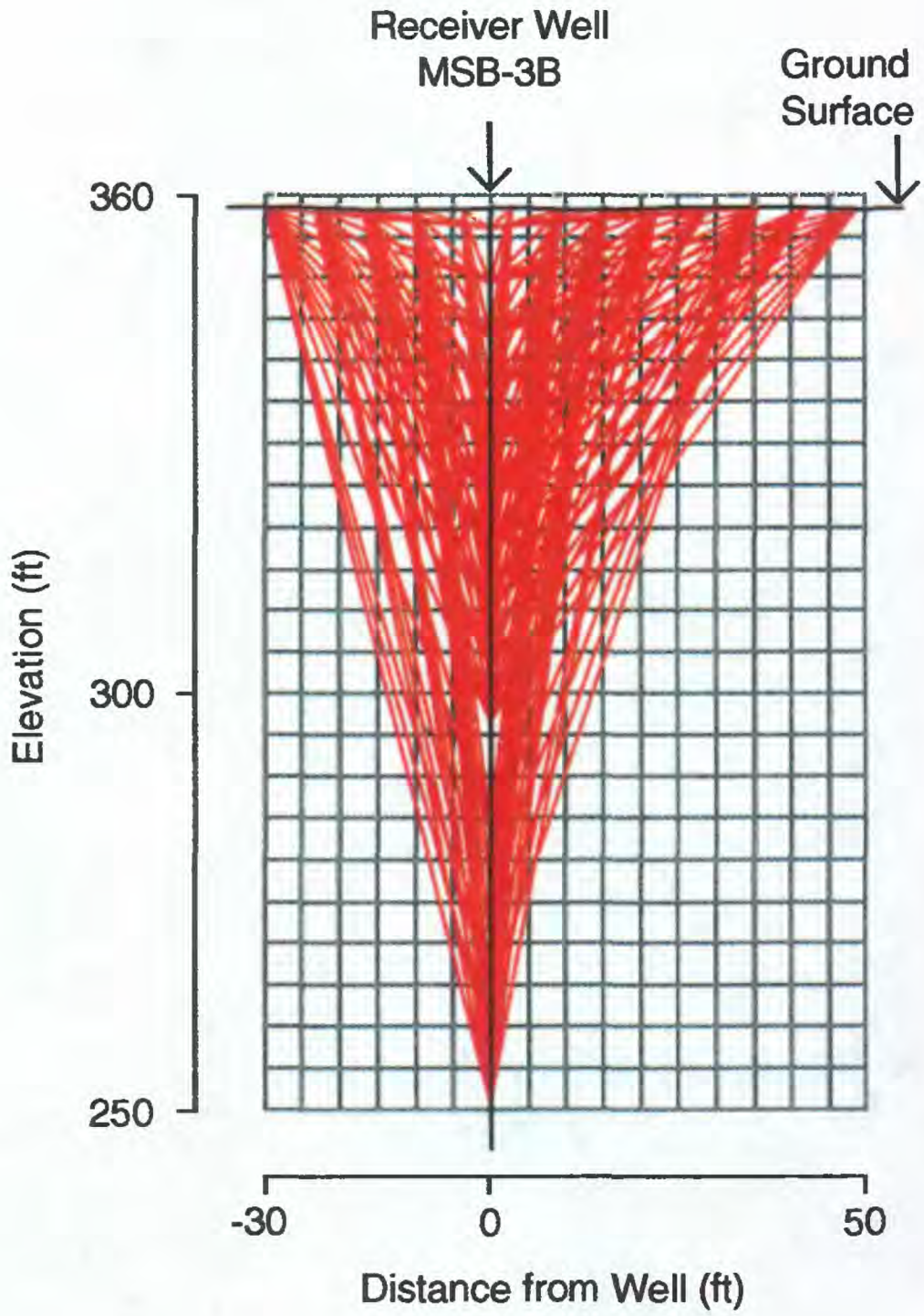

(c)

Figure 6. continued.

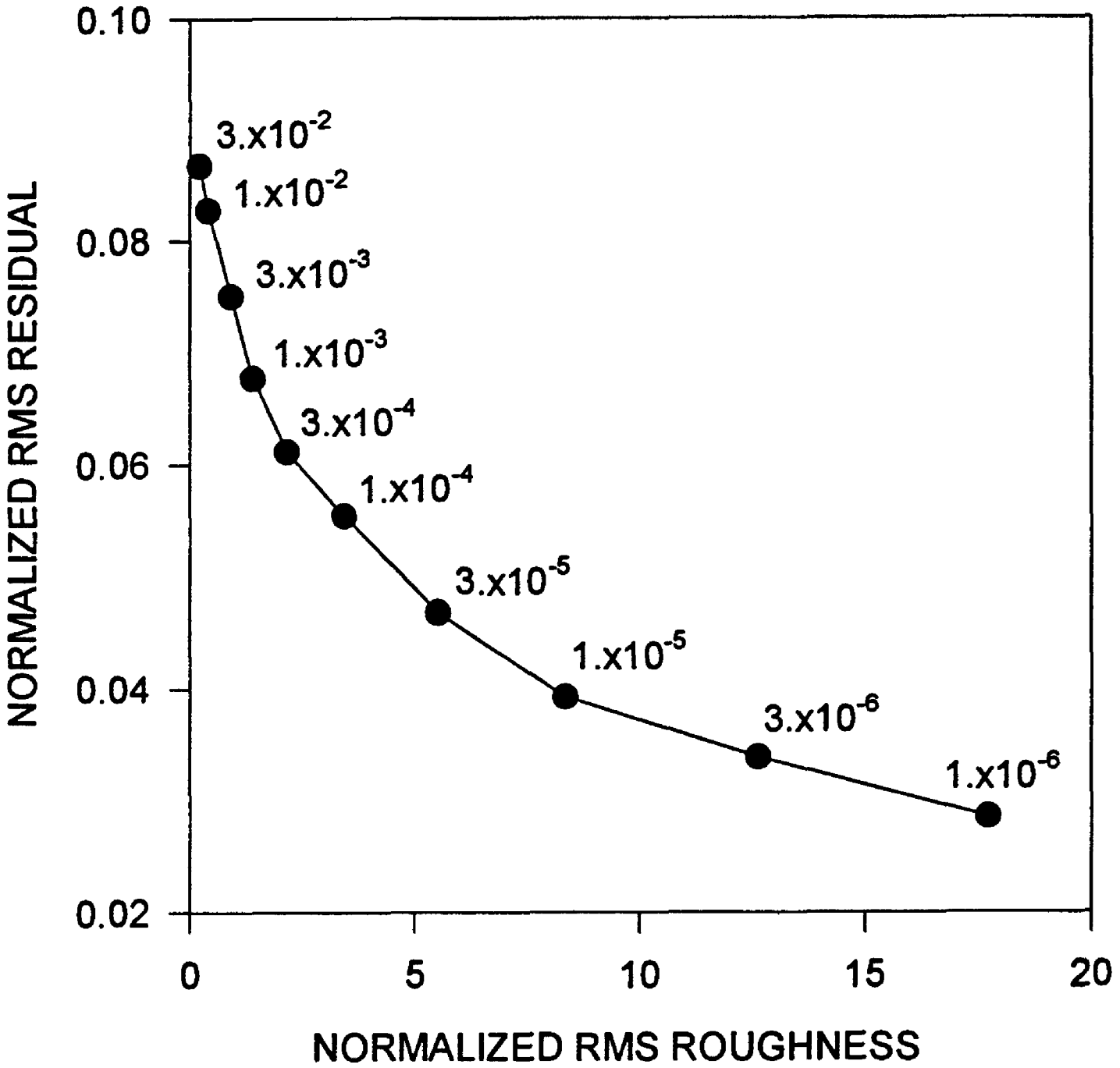

Figure 7. Trade-off curve for the (iterative reweighted least squares) inversion of the data collected in the saturated zone. The value of λ is next to the plotted point.

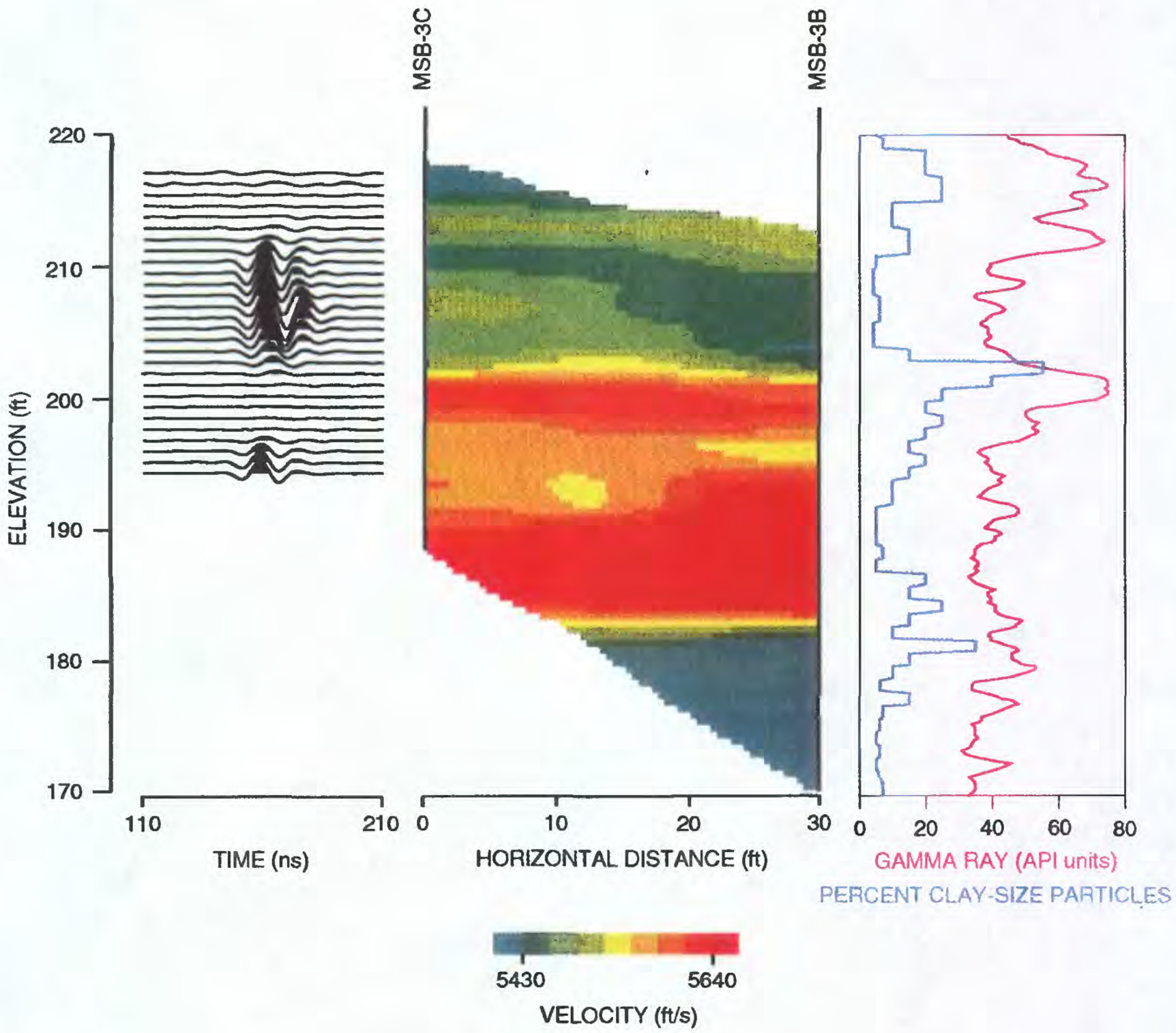

Figure 8. Seismic tomogram for the well-to-well geometry in the saturated zone and other data used for the interpretation. The tomogram pertains to the region between wells MSB-3C and MSB-3B (Figure 1b). The radar scans were collected with antennas in these two wells. The percentages of clay-size particles were measured in core taken from well MSB-3B, and the gamma ray measurements were made in well MSB-3B. A detailed explanation of these data is in section 5.1.

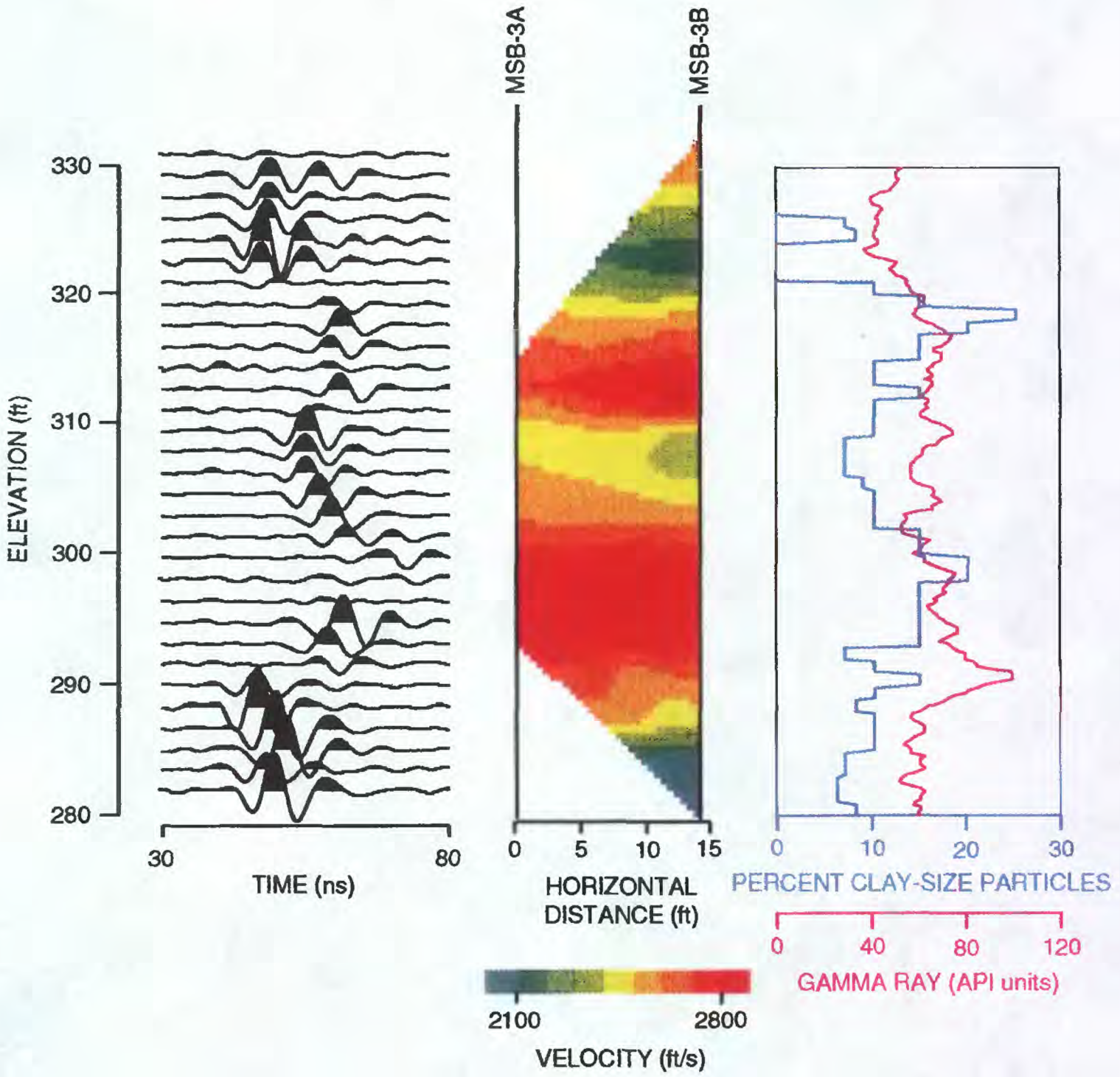

Figure 9. Seismic tomogram for the well-to-well geometry in the unsaturated zone and other data used for the interpretation. The tomogram pertains to the region between wells MSB-3A and MSB-3B (Figure 1b). The radar scans were collected with antennas in these two wells. The percentages of clay-size particles were measured in core taken from well MSB-3B, and the gamma ray measurements were made in well MSB-3B. A detailed explanation of these data is in section 5.2.

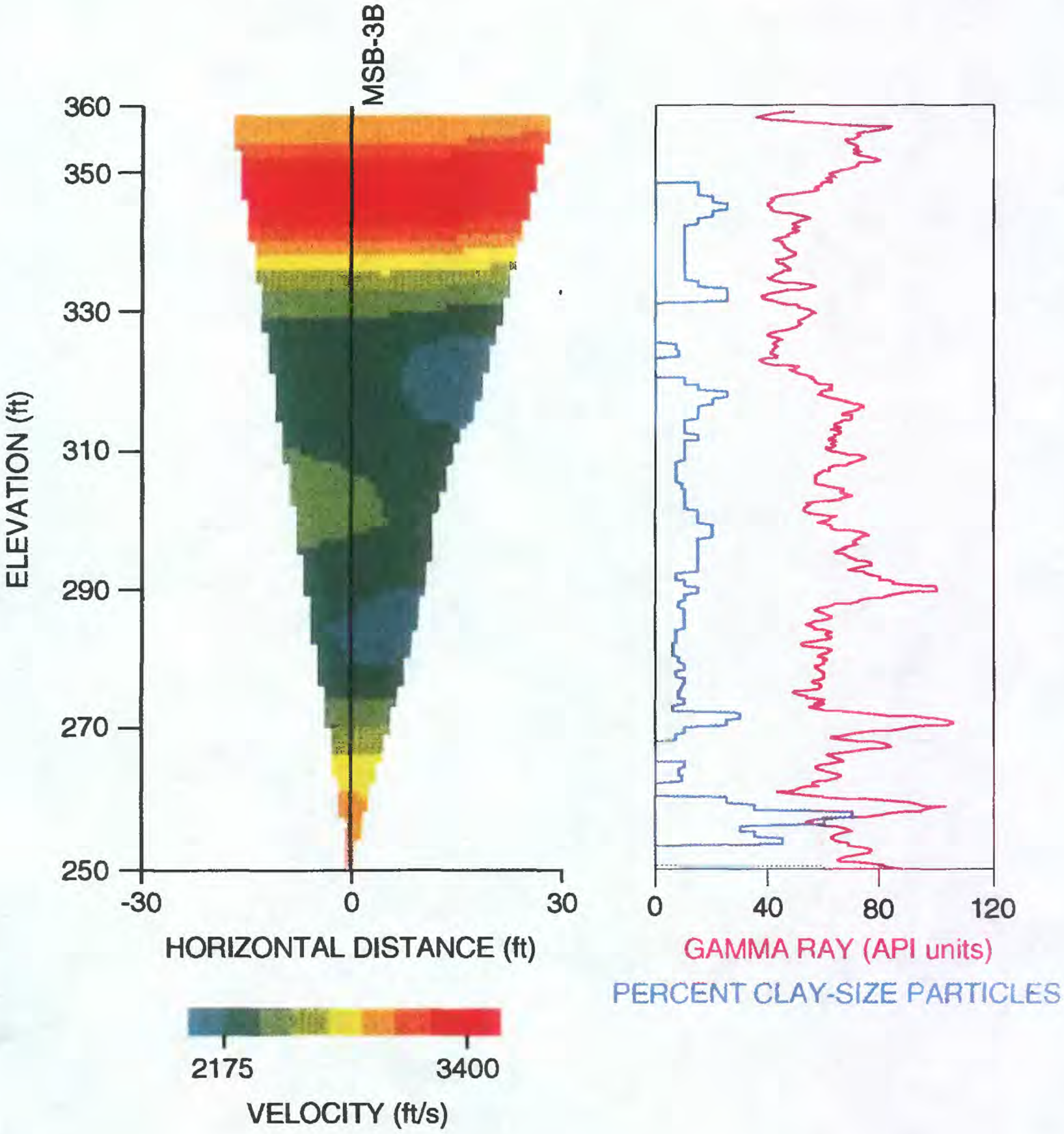

Figure 10. Seismic tomogram for the surface-to-well geometry in the unsaturated zone and other data used for the interpretation. The tomogram pertains to the region between the surface and well MSB-3B (Figure 1b). The percentages of clay-size particles are measured in core taken from well MSB-3B, and the gamma ray measurements were made in well MSB-3B. A detailed explanation of these data is in section 5.3.

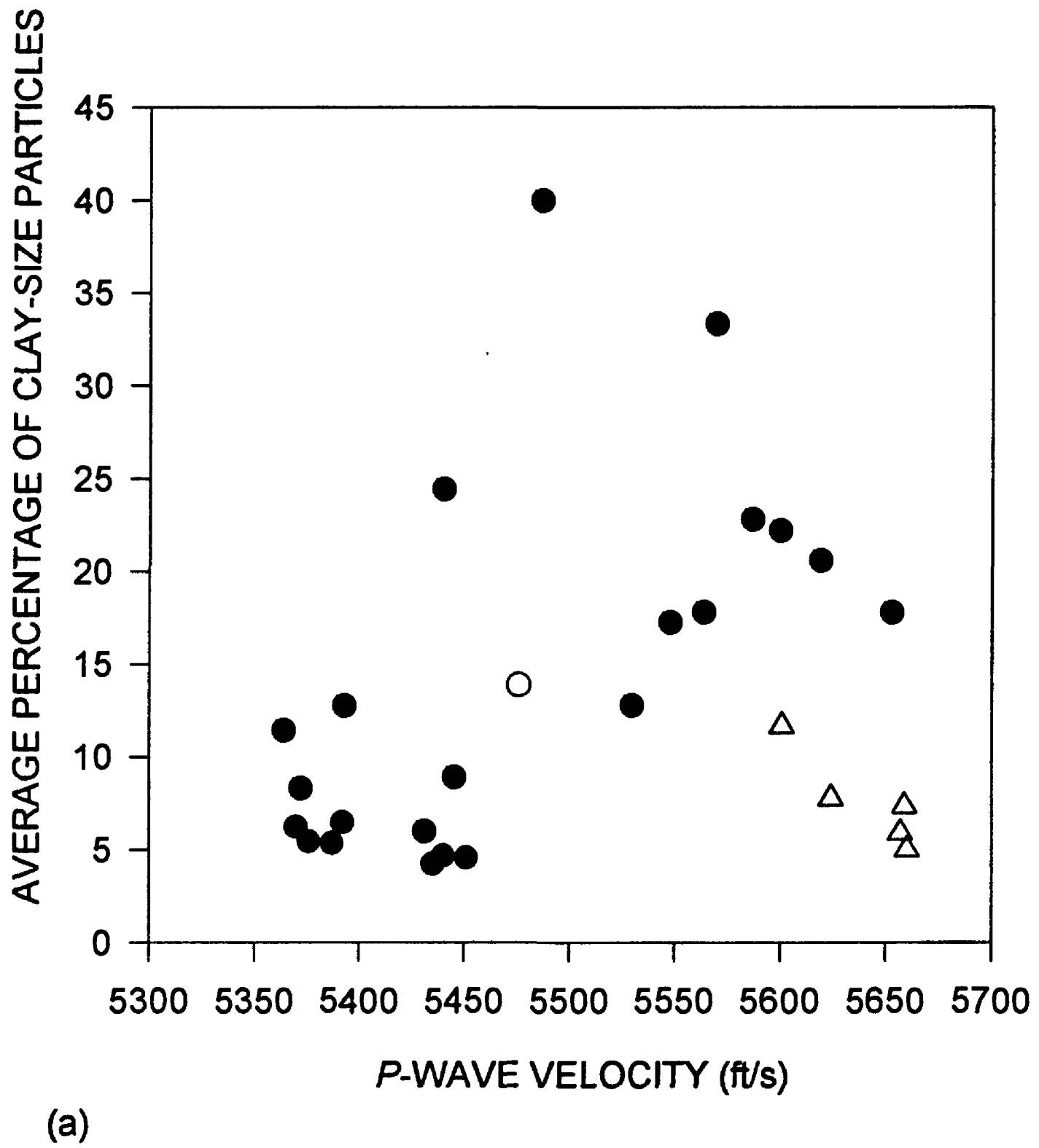

Figure 11. Relation between the *P*-wave velocities and the percentages of clay-size particles for (a) the saturated and (b) the unsaturated zones. Open circles represent unreliable velocities, which are determined from the ray diagrams (Figures 6a and 6b); open triangles velocities between 183 and 194 ft in the saturated zone; and solid circles reliable velocities outside this interval.

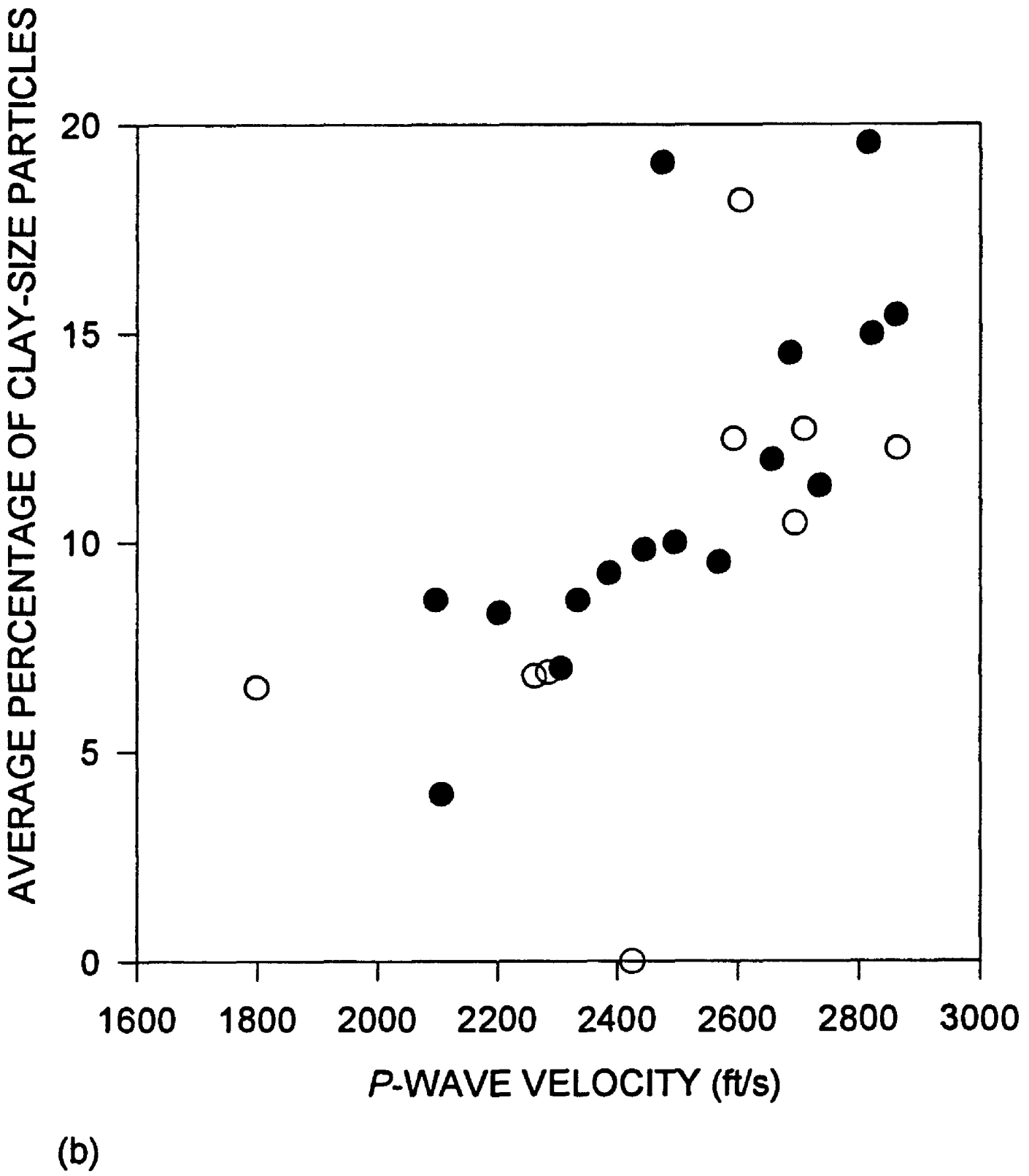

(b)

Figure 11. continued.

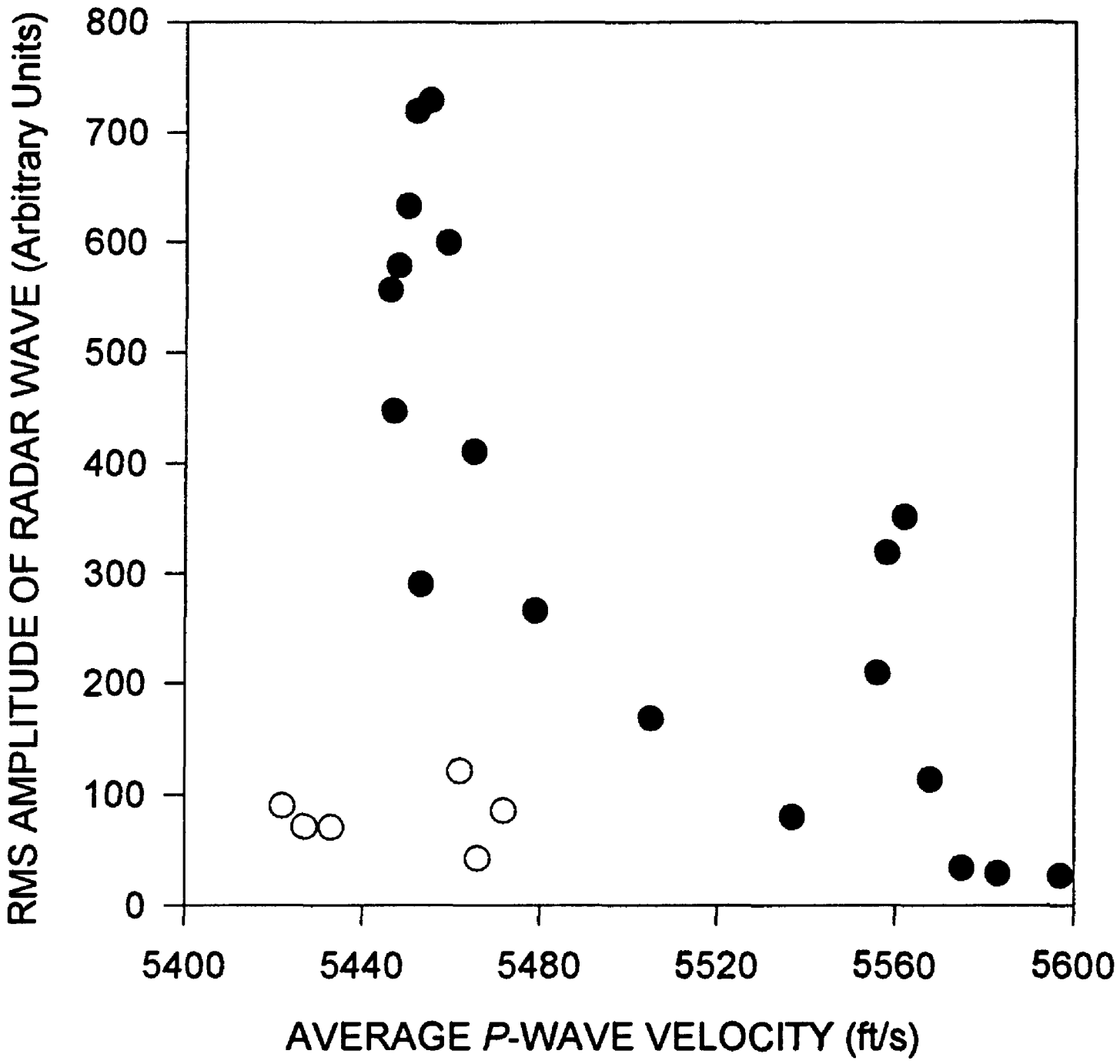

Figure 12. Relation between the *P*-wave velocities and the amplitudes of the radar waves in the saturated zone. Solid and open circles represent reliable and unreliable velocities, respectively (see Figure 6a).

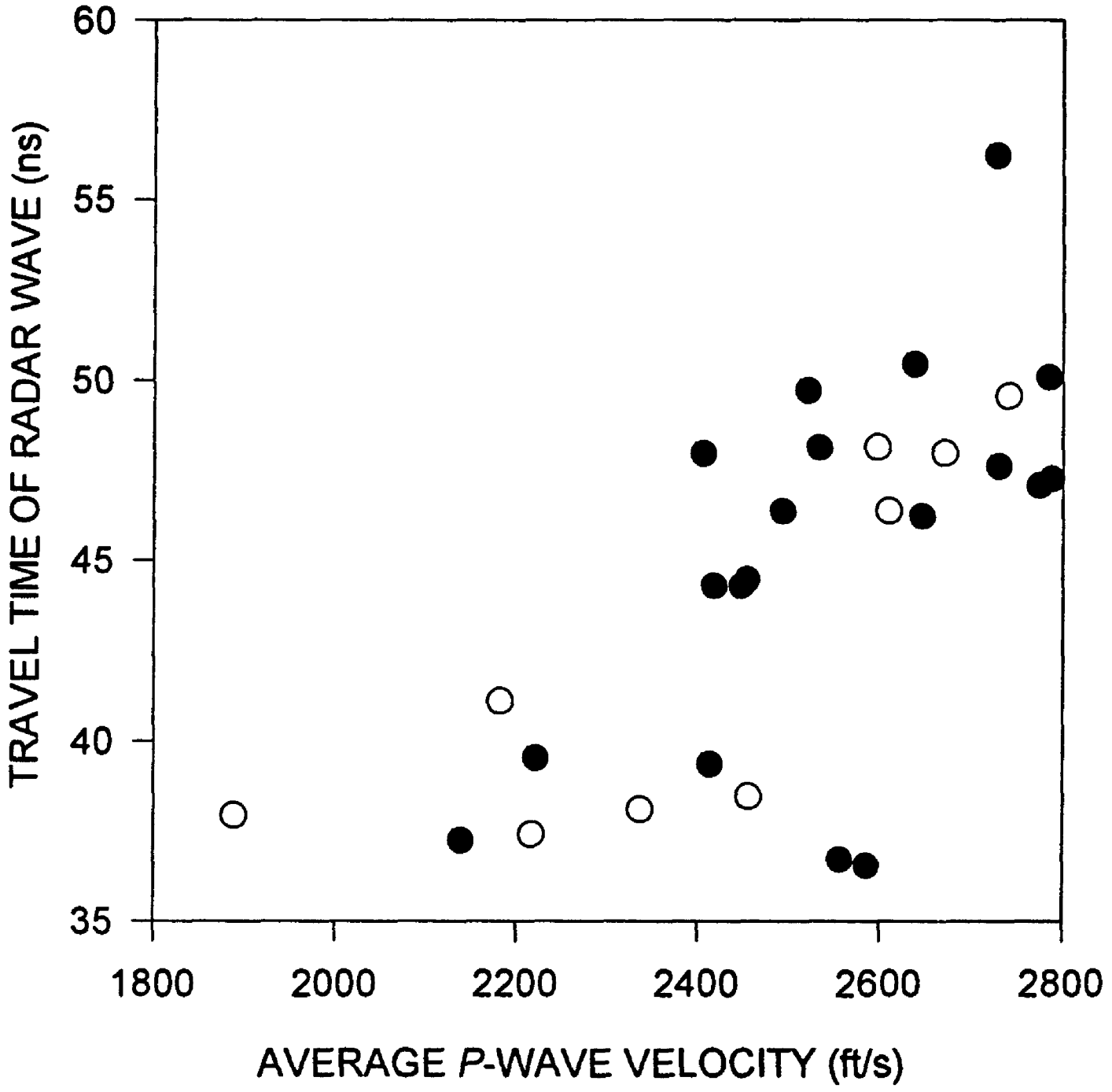

Figure 13. Relation between the *P*-wave velocities and the travel times of the radar waves in the unsaturated zone. Solid and open circles represent reliable and unreliable velocities, respectively (see Figure 6b).

APPENDIX

BOREHOLE DEVIATION DATA

Table A-1. Deviation of well MSB-3A with respect to magnetic north.

Cable Depth (m)	North-South Deviation (m)	East-West Deviation (m)
1.4	0.00	0.00
2.0	0.00	0.00
3.0	0.00	0.00
4.0	0.00	0.00
5.0	0.00	0.00
6.0	0.00	0.00
7.0	0.00	0.00
8.0	-0.01	0.00
9.0	-0.01	0.00
10.1	-0.01	0.00
11.0	-0.01	0.00
12.1	-0.01	0.00
13.0	-0.01	0.00
14.1	-0.01	0.01
15.0	-0.02	0.01
16.0	-0.02	0.01
17.1	-0.03	0.02
18.0	-0.03	0.01
19.0	-0.03	0.02
20.0	-0.03	0.02
21.1	-0.04	0.02
22.0	-0.04	0.01
23.0	-0.04	0.01
24.1	-0.04	0.01
25.1	-0.04	0.01
26.1	-0.04	0.01
27.0	-0.04	0.01
28.1	-0.03	0.01
29.1	-0.03	0.01
30.0	-0.03	0.01
31.1	-0.02	0.01
32.0	-0.01	0.02
33.1	-0.02	0.03
34.2	-0.02	0.03
35.0	-0.02	0.04
36.0	-0.01	0.05
37.0	0.00	0.05
38.1	0.01	0.04

Table A-2. Deviation of well MSB-3B with respect to magnetic north.

Cable Depth (m)	North-South Deviation (m)	East-West Deviation (m)
1.4	0.00	0.00
2.0	0.02	-0.01
3.0	0.05	-0.00
4.0	0.06	-0.01
5.0	0.02	-0.02
6.0	0.03	-0.03
7.0	0.01	0.00
8.0	-0.00	-0.03
9.0	-0.03	-0.03
10.0	-0.06	-0.04
11.0	-0.04	-0.05
12.0	-0.04	-0.02
13.1	-0.02	-0.03
14.0	-0.02	-0.01
15.0	-0.01	-0.02
16.0	0.02	-0.03
17.0	-0.01	-0.03
18.1	0.01	-0.00
19.0	0.02	0.03
20.0	0.01	0.00
21.0	0.03	0.03
22.1	0.00	0.04
23.0	-0.01	0.07
24.0	-0.02	0.04
25.0	-0.02	0.07
26.0	-0.05	0.08
27.0	-0.03	0.10
28.0	-0.01	0.09
29.0	-0.01	0.06
30.0	0.02	0.06
31.0	-0.01	0.07
32.1	0.02	0.09
33.0	-0.01	0.09
34.0	-0.01	0.06
35.1	0.00	0.04
36.0	-0.03	0.03
37.0	-0.05	0.02
38.0	-0.04	-0.00
39.1	-0.02	-0.03
40.0	0.00	-0.01
41.0	0.03	0.01
42.0	0.01	-0.01
43.1	0.04	0.01

Table A-2 (continued). Deviation of well MSB-3B wth respect to magnetic north.

Cable Depth (m)	North-South Deviation (m)	East-West Deviation (m)
45.0	0.09	-0.03
46.0	0.12	-0.03
47.0	0.14	-0.05
48.0	0.16	-0.03
49.0	0.14	-0.01
50.0	0.12	0.02
51.0	0.09	0.02
52.0	0.07	0.01
53.0	0.08	-0.01
54.0	0.06	0.02
55.0	0.03	0.03
56.0	0.04	0.01
58.0	0.09	-0.01
59.0	0.10	0.01
60.1	0.07	0.01
61.0	0.09	0.02
62.0	0.06	0.03
63.0	0.04	0.01
64.0	0.06	-0.02
65.0	0.03	-0.03
66.0	0.06	-0.01
67.0	0.03	0.00
68.0	-0.03	0.01
69.0	-0.09	0.02

Table A-3. Deviation of well MSB-3C with respect to magnetic north.

Cable Depth (m)	North-South Deviation (m)	East-West Deviation (m)
2.0	0.00	0.00
3.0	-0.01	0.00
4.0	0.00	-0.01
4.9	0.00	-0.01
6.1	0.01	-0.01
7.0	0.00	-0.02
8.1	0.00	-0.03
9.0	-0.00	-0.02
10.0	-0.01	-0.02
11.1	-0.01	-0.03
12.0	-0.01	-0.04
13.0	-0.01	-0.04
14.0	-0.01	-0.04
15.0	-0.02	-0.04
16.0	-0.02	-0.03
17.1	-0.02	-0.03
18.0	-0.03	-0.03
19.0	-0.02	-0.04
20.0	-0.02	-0.03
21.0	-0.02	-0.03
22.0	-0.02	-0.03
23.1	-0.03	-0.03
24.0	-0.03	-0.03
25.0	-0.03	-0.03
26.0	-0.03	-0.03
27.1	-0.03	-0.04
28.0	-0.02	-0.03
29.0	-0.02	-0.03
30.0	-0.02	-0.04
31.1	-0.02	-0.04
32.0	-0.02	-0.03
33.1	-0.02	-0.03
34.1	-0.02	-0.04
35.0	-0.02	-0.04
36.0	-0.01	-0.04
37.1	-0.01	-0.03
38.1	-0.01	-0.02
39.2	-0.02	-0.02
40.0	-0.02	-0.03
41.0	-0.03	-0.03
42.0	-0.03	-0.01

Table A-3 (continued). Deviation of well MSB-3C with respect to magnetic north.

Cable Depth (m)	North-South Deviation (m)	East-West Deviation (m)
43.0	-0.03	-0.02
44.0	-0.03	-0.02
45.0	-0.02	-0.03
46.0	-0.02	-0.04
47.0	-0.03	-0.04
48.0	-0.02	-0.05
49.0	-0.02	-0.05
50.0	-0.01	-0.04
51.1	-0.02	-0.04
52.0	-0.02	-0.04

Table A-4. Deviation of well MSB-3D with respect to magnetic north.

Cable Depth (m)	North-South Deviation (m)	East-West Deviation (m)
3.0	0.00	0.00
4.0	-0.01	0.00
5.0	-0.01	0.00
6.0	-0.02	-0.01
7.0	-0.03	-0.02
8.0	-0.06	-0.03
9.0	-0.07	0.00
10.0	-0.06	-0.02
11.2	-0.02	-0.03
12.0	-0.03	0.00
13.0	-0.01	-0.02
14.0	0.01	-0.02
15.0	0.04	-0.02
16.0	0.06	0.00
17.0	0.09	0.00
18.0	0.10	-0.01
19.0	0.12	-0.03
20.0	0.11	-0.04
21.1	0.14	-0.03
22.0	0.12	-0.02
23.0	0.12	0.01
24.0	0.12	0.04
25.0	0.14	0.02
26.1	0.16	0.04
27.1	0.18	0.02
28.0	0.18	0.01
29.0	0.17	0.00
30.0	0.16	-0.01
31.0	0.18	0.02
32.0	0.17	0.01
33.0	0.16	0.00
34.1	0.16	-0.01
35.0	0.16	-0.02
36.0	0.17	-0.04
37.0	0.18	-0.06

Table A-5. Deviation of well MSB-22 with respect to magnetic north (run no. 1).

Cable Depth (m)	North-South Deviation (m)	East-West Deviation (m)
1.4	0.00	0.00
2.0	0.00	-0.02
3.0	0.02	-0.06
4.0	0.05	-0.08
5.0	0.02	-0.11
6.0	0.03	-0.07
7.0	0.01	-0.10
8.0	0.04	-0.12
9.0	0.08	-0.12
10.0	0.05	-0.10
11.0	0.01	-0.12
12.0	0.01	-0.09
13.0	-0.02	-0.13
14.0	-0.04	-0.10
15.0	-0.06	-0.15
16.0	-0.10	-0.18
17.0	-0.11	-0.23
18.0	-0.15	-0.27
19.2	-0.13	-0.33
20.0	-0.13	-0.32
21.0	-0.16	-0.37
22.1	-0.21	-0.41
23.0	-0.22	-0.37
24.0	-0.19	-0.42
25.0	-0.24	-0.39
26.0	-0.29	-0.41
27.1	-0.29	-0.39
28.0	-0.29	-0.37
29.0	-0.33	-0.34
30.1	-0.40	-0.38
31.1	-0.40	-0.36
32.0	-0.41	-0.33
33.0	-0.47	-0.36
34.0	-0.52	-0.38
35.0	-0.53	-0.44
36.0	-0.53	-0.50
37.0	-0.54	-0.48

Table A-6. Deviation of well MSB-22 with respect to magnetic north (run no. 2).

Cable Depth (m)	North-South Deviation (m)	East-West Deviation (m)
3.6	0.00	0.00
4.0	-0.01	0.00
6.0	0.02	0.02
8.1	-0.01	0.05
10.0	0.02	0.06
12.0	0.04	0.04
14.0	0.08	0.06
16.0	0.10	0.05
18.0	0.10	0.04
20.0	0.09	0.02
22.0	0.08	0.09
24.0	0.13	0.08
26.0	0.11	0.06
28.0	0.15	0.04
30.1	0.18	0.00
32.0	0.21	0.01
34.0	0.21	0.08
36.1	0.24	0.06
37.0	0.23	0.05

Table A-7. Deviation of well MSB-58D with respect to magnetic north.

Cable Depth (m)	North-South Deviation (m)	East-West Deviation (m)
2.0	0.00	0.00
3.0	0.00	0.00
4.0	0.00	0.00
5.0	0.00	0.00
6.0	0.00	0.00
7.0	0.00	0.00
8.0	0.00	0.00
9.0	0.00	0.00
10.1	0.00	0.00
11.0	0.00	0.00
12.0	0.00	0.00
13.0	0.00	0.00
14.0	0.01	0.00
15.0	0.01	0.00
16.0	0.01	0.00
17.1	0.01	0.00
18.0	0.01	0.00
19.0	0.01	-0.01
20.0	0.01	-0.01
21.1	0.01	-0.01
22.1	0.00	-0.01
23.0	0.00	0.00
24.0	0.00	0.00
25.0	0.00	0.00
26.0	0.00	0.01
27.0	0.00	0.00
28.1	-0.01	0.00
29.0	0.00	0.00
30.0	-0.01	-0.02
31.1	-0.01	0.00
32.0	-0.01	-0.02
33.0	0.01	-0.02
34.0	0.03	-0.03
35.0	0.04	-0.05
36.0	0.03	-0.07
37.1	0.05	-0.06
38.0	0.03	-0.06
39.0	0.06	-0.06
40.0	0.06	-0.09
41.0	0.09	-0.07
42.0	0.10	-0.03
43.1	0.12	0.00
44.0	0.15	0.00